THESIS

TROPICAL TROPOPAUSE LAYER VARIABILITY ASSOCIATED WITH THE

MADDEN-JULIAN OSCILLATION DURING DYNAMO

Submitted by

Erin L. Dagg

Department of Atmospheric Science

Master's Committee:

    Advisor: Thomas Birner
    Co-Advisor: Richard H. Johnson

    Wayne H. Schubert
    Michael Kirby

ABSTRACT

TROPICAL TROPOPAUSE LAYER VARIABILITY ASSOCIATED WITH THE

MADDEN-JULIAN OSCILLATION DURING DYNAMO

As the transition region between the troposphere and stratosphere, the tropical tropopause layer (TTL) has importance as the gateway to the stratosphere for atmospheric tracers such as water vapor. This has implications for Earth's radiative budget and climate. Observations in this region show time variations across multiple scales that are not fully understood, including the intraseasonal variability of the Madden-Julian oscillation (MJO). In this study, we investigate the evolution of TTL properties and their vertical structure during the Dynamics of the Madden-Julian Oscillation (DYNAMO) field campaign from October-December 2011. This time period is particularly interesting in that two prominent MJO passages were seen over the tropical Indian Ocean.

We focus analysis on two equatorial sites. Gan Island, Maldives (0.7° S, 73.2° E) provides a better understanding of the response of the TTL to MJO dynamics in the region of initiation. Manus Island, Papua New Guinea (2.1° S, 147.4° E) observations portray a later stage of the MJO during its eastward propagation. We use multiple datasets, including high vertical resolution, three-hourly atmospheric soundings over the three-month period. CALIPSO satellite data is additionally used in determining the presence of thin cirrus clouds and their impact on radiative heating rates. Characteristics of the broadscale structure of the MJO are analyzed, as well as higher-frequency variations of the flow near the TTL accompanying an increase in MJO-related deep convective clouds. Spectral filtering is used to isolate low-frequency variability, Kelvin wave activity, and higher-frequency gravity wave perturbations.

A 7-20 day bandpass of the temperature and zonal wind fields reveals strong Kelvin wave signals in late October and early December. This Kelvin wave response to large-scale convection exhibits a downward phase velocity consistent with an eastward-propagating energy source below. The descending cold phase between 100-150 hPa coincides with a lowering of the cold point tropopause and an increase in cirrus cloud frequency preceding the active phase of the MJO. The wave signals dissipate before reaching Manus Island, suggesting that the MJO may have decoupled from convection. Further analysis shows lower stratospheric gravity wave activity does not appear to be modulated by the MJO, but is generally stronger at Manus Island due to its proximity to the west Pacific warm pool.

ACKNOWLEDGEMENTS

DEDICATION

This thesis is dedicated to my parents,

who have shown endless love and support

throughout my studies.

TABLE OF CONTENTS

LIST OF FIGURES

CHAPTER 1

Introduction

1.1. The tropical tropopause layer

Stratospheric water vapor is an important greenhouse gas and contributes to warming of the Earth's atmosphere. In addition to a direct radiative forcing, increases in concentration are predicted to lead to a loss of ozone and changes in global circulation. Recent research by Solomon et al. (2010) looks at trends in the past few decades. Observations of lower stratospheric water vapor show a steady rise from 1980 to 2000, which likely contributed to the global warming associated with the increase in anthropogenic greenhouse gas emissions. More recently, stratospheric concentrations showed a large drop in 2000 followed by a period where concentrations seemed to level off. This has sparked an interest in what causes these changes in stratospheric water vapor and what that means for us in the coming years.

Oxidation of methane is one source of water vapor in the stratosphere. However, the most important influence on stratospheric water vapor is vertical transport from lower levels. For water to make it from the troposphere to the stratosphere, it must cross the atmospheric boundary known as the tropopause. In recent years, it has become evident that this interface is a transition region rather than a clearly defined level. Observations suggest a layer extending over several kilometers that shares characteristics of both the troposphere and stratosphere, with a time-varying structure related to radiative, dynamical, and chemical processes. In the tropics, this transition region is known as the tropical tropopause layer (TTL). Fueglistaler et al. (2009) gives a broad overview of the TTL, suggesting an upper boundary at 70 hPa, and lower boundary at 150 hPa, above the level of main convective outflow.

Figure 1.1 summarizes the general processes and properties of the TTL. Conventional definitions of the tropopause are based on the thermal structure of the atmosphere, shown by the green line. As the transition region between the troposphere and stratosphere, the tropical tropopause layer has a mean vertical temperature profile that decreases with height until a certain level and then increases. The cold point tropopause (CPT), determined by this temperature minimum, is typically near 90 hPa and has a temperature around 190 K. The lapse rate tropopause (LRT) indicates a transition in atmospheric stability and is characteristically near 100 hPa (Fueglistaler et al. 2009). Since lapse rate is not a conservative quantity, alternate ways to define the tropopause include a dynamic tropopause based on potential vorticity in the extratropics (Andrews et al. 1987), as well as definitions based on chemical compositions such as ozone or water vapor.
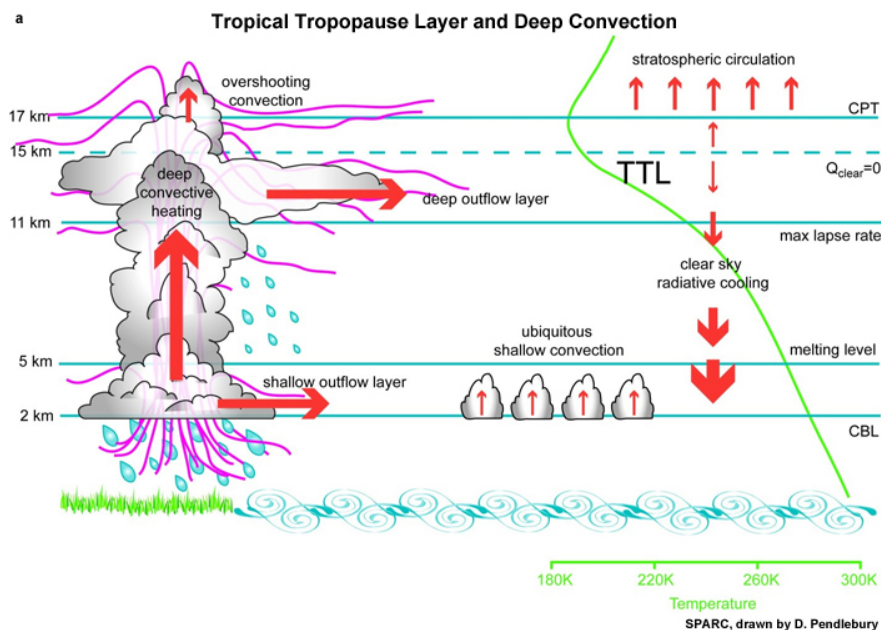
FIGURE 1.1. Schematic summarizing the properties and processes of the tropical tropopause layer, including the mean temperature profile, overshooting convection, and the large-scale Brewer-Dobson circulation. From Barth et al. (2007).

Studies of the TTL continue in order to better understand troposphere-stratosphere exchange. There is a strong relationship between cold point tropopause temperature and the entry of water vapor into the stratosphere. The phase changes from vapor to liquid or ice are controlled by the temperature, with colder temperatures leading to greater dehydration. This means that the seasonal cycle in tropopause temperatures results in a seasonal cycle of absolute humidity and affects how much is advected to upper levels, a pattern sometimes referred to as the "atmospheric tape recorder" (Mote et al. 1996). Tropical tropopause temperatures are the lowest from January-March (boreal winter), when tropical upwelling is the strongest.

Tropopause characteristics are vastly different across the globe. There is a strong meridional temperature gradient with the coldest temperatures and highest heights in the tropics. Differences are found across longitudes as well, with minimum temperatures located over the western Pacific warm pool, near 170° E. These spatial patterns can be seen in Figure 1.2 taken from Fueglistaler et al. (2009), which show both the January and July monthly averages. In July, there is an extension of the temperature minimum over the Indian and Southeast Asian monsoon region. Winds and geopotential height anomalies are also shown, and look quite different depending on the time of year. In general, we expect prevailing easterlies in the tropics as are seen in July. During this time there is also a large anticyclone centered over southeast Tibet. In contrast we see Rossby gyres over the western Pacific Ocean that are symmetric about the equator during boreal winter.

The tropics happen to be the most important region for vertical mass transport due to the Brewer-Dobson circulation. This wave-driven circulation is characterized by large-scale upwelling in the tropics where air enters the stratosphere through the TTL, undergoes equator-to-pole transport, and experiences subsidence at higher latitudes (Holton et al.
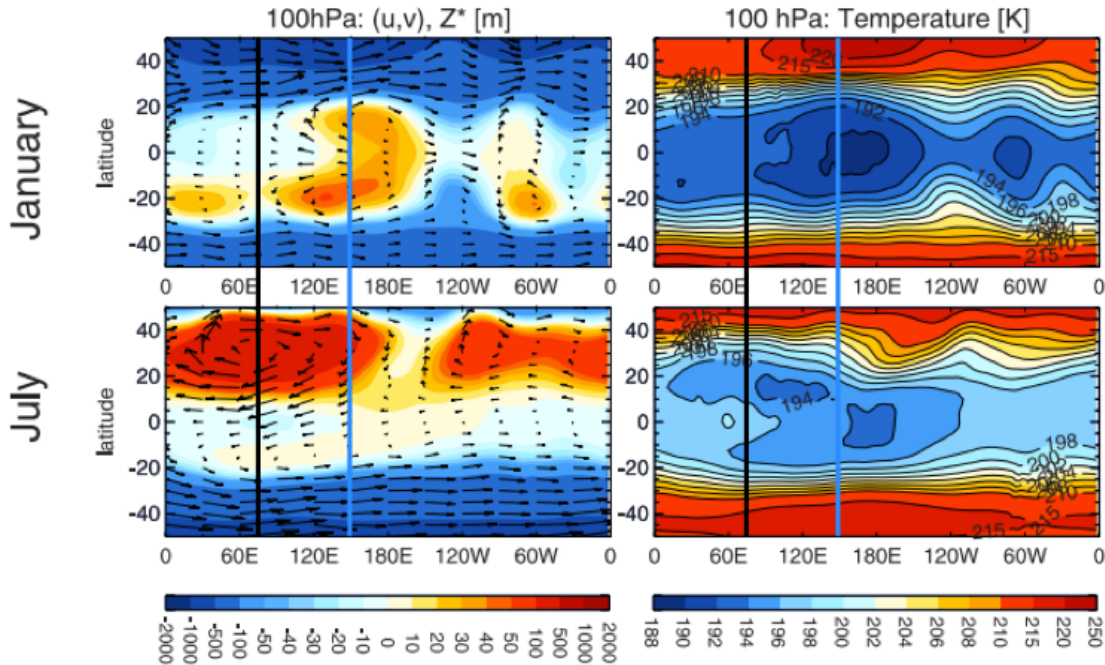
FIGURE 1.2. 100 hPa maps of January and July mean fields for [left] wind (vector field) and geopotential height anomaly relative to 10°S-10°N mean and [right] temperature (ERA-40, averaged 1990-2000). From Fueglistaler et al. (2009). For reference, solid vertical lines mark the longitude of Gan Island (black) and Manus Island (blue).

1995). The strong seasonal cycles in tropopause temperature and height are associated with the Brewer-Dobson circulation and upwelling at the tropics. The tropics are also of interest in that it is a convectively active region due to the warmer sea surface temperatures and the proximity to the inter-tropical convergence zone.

The processes that control stratospheric water vapor include the effects of clouds, and variations in vertical transport are often associated with the distribution of deep convection. Convection can lead to moistening of the stratosphere by penetrating the TTL and transporting water vapor to stratospheric heights. The cold temperatures near the TTL can also lead to supersaturation with respect to ice. Clouds that are able to form at this altitude are primarily cirrus clouds composed of ice crystals and can lead to dehydration through freeze-drying (Jensen et al. 1996). Sassen et al. (2008) describe the spatial and seasonal trends in

cirrus clouds. A higher occurrence is typically found in the western Pacific where tropopause temperatures are colder and convection is frequent. There is a strong seasonal cycle reaching a maximum in boreal winter. Although water vapor concentrations are generally very low above 200 hPa, they play a significant role in the radiative budget of the stratosphere. Cirrus clouds are optically thin and have only a small effect on incoming solar radiation, but can strongly reduce the outgoing infrared radiation through absorption. As such, the air above a cirrus cloud will experience lower temperatures, while there is a significant heating (greater than 5 K) near the cloud base (Liou 1986). When present, the net warming will lead to a lowering of the level of zero net radiative heating (Corti et al. 2005). The level of zero net radiative heating (LZRH) is the height at which there is a transition from a net radiative cooling below to radiative heating above and is typically near 15 km under clear sky conditions. This level is important for troposphere-stratosphere transport, as radiative cooling below means that air will likely sink back down into the troposphere. Air above this level cools adiabatically while being lofted, which is balanced by radiative heating, and will continue to rise.

Convection can play a direct role in TTL dynamics by exciting waves in the TTL and lower stratosphere, where high stratification amplifies wave propagation. Atmospheric Kelvin waves are characterized by oscillations in variables such as winds, pressure, and temperature. In particular, we expect a quadrature phase relationship between zonal wind and temperature from linear wave theory. Waves can either be free or forced modes, with the main atmospheric forcing in the tropics being diabatic heating from convection as an energy source. A downward tilted vertical structure is a result of upward energy dispersion generated by a moving convective heat source below.

Using observations of outgoing longwave radiation (OLR) in the tropics, Wheeler and Kiladis (1999) plotted wavenumber-frequency spectral peaks showing that variability falls along the theoretical dispersion curves for equatorial waves. Matsuno (1966) was the first to solve the linearized shallow-water equations of motion on the equatorial β-plane. Equatorial waves modes are trapped near equator, with propagation only in the zonal and vertical directions. These include Kelvin, equatorial Rossby, inertio-gravity, and mixed Rossby-gravity waves. Kelvin waves are characterized by eastward propagation, and relatively fast propagating dry modes are primarily found in the stratosphere. Convective heating reduces the effective stratification of the layer, so that convectively-coupled waves are slower with a phase speed around 12-18 m s^{-1}. Rossby waves have roughly a third of the speed of Kelvin waves and propagate westward, though their group velocity (energy) may be either be in the eastward or westward direction. A broad spectrum of higher frequency gravity waves have both westward and eastward energy propagation.

With climate change, the troposphere is expected to warm while the stratosphere is expected to cool. What this means for the interface at the tropical tropopause layer and how it will impact stratospheric water vapor concentration is uncertain. Interannual variability of temperatures in the TTL are linked to the El Niño-Southern Oscillation (ENSO), volcanic eruptions, and temperature changes resulting from the quasi-biennial oscillation (QBO) in stratospheric winds, and are typically on the order of 1 K. The QBO is an oscillation of zonal wind regimes in the equatorial stratosphere (10-100 hPa) with a mean period of 28 months. Wind regimes descend at a rate of roughly 1 km month^{-1} with dissipation at the tropical tropopause (Baldwin et al. 2001). Approximately two year variations associated with the QBO are found in tropopause height and temperature, as well as lower stratospheric water vapor (Randel et al. 2000). While there is significant variability on these timescales,

changes in stratospheric water vapor is seen on shorter timescales that are not fully under-stood. Phenomena such as the Madden-Julian oscillation can modulate TTL thermodynamic properties, and result in water vapor and ozone feedbacks.

1.2. The Madden-Julian oscillation and its influence on the TTL

One phenomenon influencing the tropical tropopause layer and vertical transport is the intraseasonal disturbance commonly referred to as the Madden-Julian oscillation (MJO). Basic characteristics and the observed features most relevant to this study are summarized below. For further reading, Zhang (2005) provides a comprehensive review of the MJO.

The Madden-Julian oscillation is the dominant component of intraseasonal variability in the tropics with a period of 30-60 days. The active phase is defined by a deep convective center and heavy precipitation, with variations in zonal winds and sea level pressure. The general circulation associated with the MJO resembles the Matsuno-Gill response to tropical heating (Matsuno 1966; Gill 1980). In this model, a Kelvin wave develops to the east of the heat source in the lower troposphere and cyclonic Rossby gyres develop to the west. As such, surface air flows towards enhanced convection in the zonal direction, with easterly flow to the east and westerly flow to the west. This leads to convergence at low levels ($\sim$850 hPa) and divergence in the upper troposphere ($\sim$200 hPa).

Slow eastward propagation of the convective center and associated atmospheric circula-tions has an average speed of 5 m s^{-1}. Eastward movement is a result of moisture availability, with prevailing easterly winds in the tropics feeding moisture to the east (ahead) of MJO-enhanced convection. An inactive phase follows close behind, as the Rossby gyres bring in dry air and suppress convection to the west. During development, the MJO is convectively-coupled and travels along the equator from the central Indian Ocean to the western Pacific.

As the active phase continues into the central and eastern Pacific Ocean, convection dissipates due to lower sea surface temperatures. This transition from the convective phase to the dry phase of the MJO allows for faster propagation once the MJO is decoupled from convection.

Work by Madden and Julian (1971, 1972) first described this oscillation with changing convective organization and a large-scale circulation in the equatorial zonal plane. To summarize, they presented an idealized lifecycle of the MJO differentiated into eight phases. The 1972 schematic is reproduced here as Figure 1.3, and is still considered to be an accurate representation of the successive phases of the Madden-Julian oscillation. Time progresses downwards, with each lettered panel depicting a phase with an interval of approximately 5 days. The various stages of cumulus clouds indicate the location of convection, and streamlines are used to show the associated anomalous circulation. The progression of mean sea level pressure anomalies and relative tropopause heights are marked as well.

Initiation begins with a surface low pressure anomaly over East Africa and the western Indian Ocean, with large-scale convection forming over the central Indian Ocean (panel F). Atmospheric circulations start to develop, with convergence at low levels and divergence aloft leading to rising motion in the convective region. With time, MJO-enhanced convection strengthens and propagates eastward along with the circulation patterns and the surface low pressure anomaly (panels G,H,A). As convection reaches the central Pacific Ocean, it starts to weaken. Furthermore, subsidence is seen in the western circulation cell signaling the suppressed phase of the MJO in that region (panel B). At this point, the MJO active phase decouples from convection completely, though signals are still seen in the circulation (panels D,E).
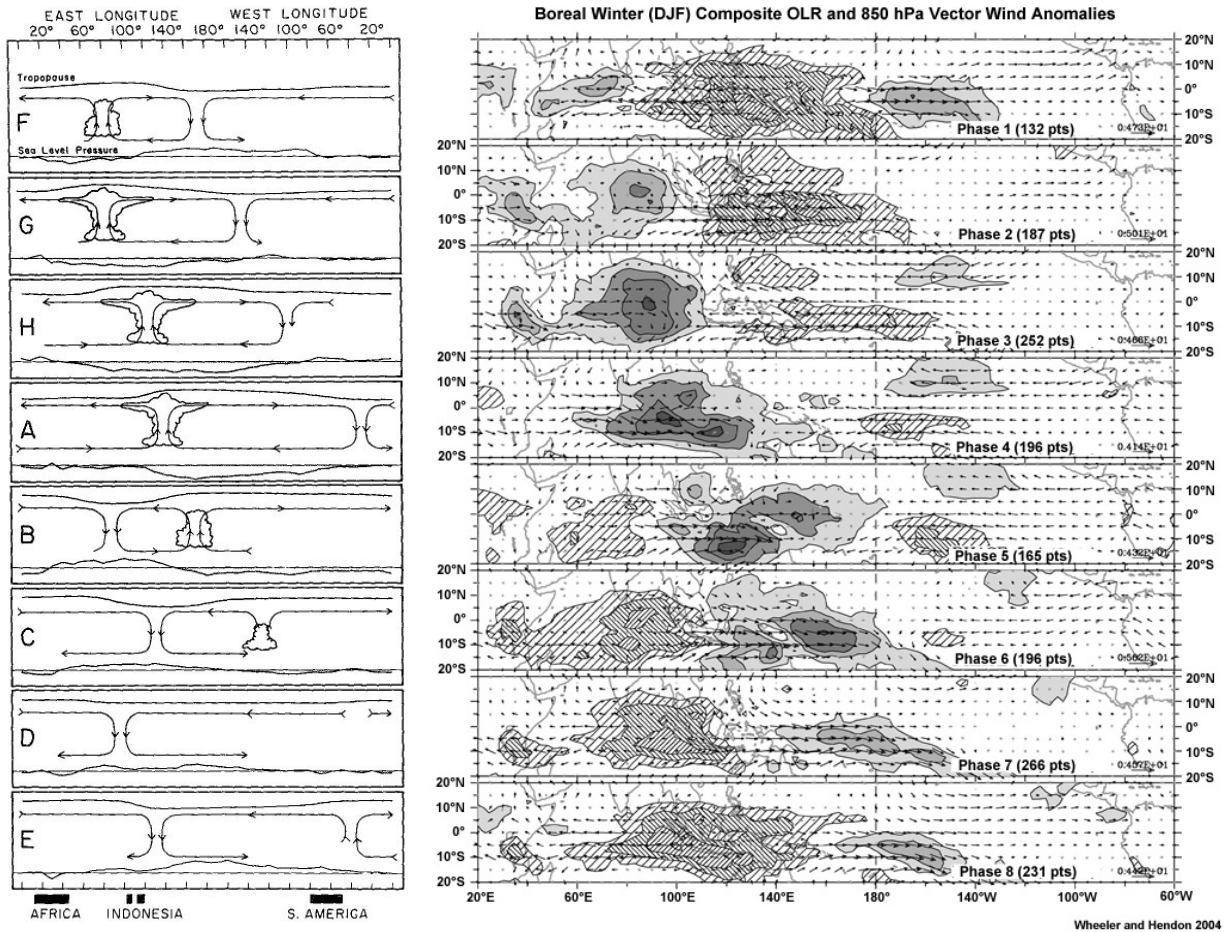
FIGURE 1.3. [Left] Equatorial cross-section showing an idealized lifecycle of the MJO, including tropopause height, convection, zonal circulation, and sea level pressure anomalies during the eastward propagation across the Indian and Pacific Oceans. From Madden and Julian (1972). [Right] Boreal winter (DJF) composite OLR and 850 hPa vector wind anomalies. Hatching (shading) levels denote OLR anomalies greater (less) than positive (negative). Statistically significant vector wind anomalies are plotted, with the magnitude of the largest vector shown on the bottom right of each panel. Phases correspond to the phases in Figure 2.2. From Wheeler and Hendon (2004).

For comparison, observations for each phase of the MJO are shown on the right. This figure was produced by Wheeler and Hendon (2004) using a composite of boreal winter (December-February) 850 hPa winds and outgoing longwave radiation (OLR). OLR is assumed to be a reasonable proxy for deep convection. In comparing the two figures, it is remarkable how well the observations of convection match for each phase of the MJO, in terms of both location and growth.

There is no consensus for the driving mechanisms behind MJO initiation and evolution, making this an active area of research. Proposed theories can be grouped into two broad categories. One idea is that the MJO is internally forced and provides its own energy source through feedback processes. This would include theories based on boundary layer moisture convergence and surface evaporation feedbacks. These theories rely on local sources of instability that support the convective growth and circulation patterns seen with the MJO. Sobel and Maloney (2013) suggest that the MJO is a moisture mode destabilized by radiative and wind-evaporative feedbacks and is propagated eastward by horizontal advection. The second group of initiation theories comes from the perspective that the MJO is an externally forced phenomenon. This idea involves interactions between the tropics and midlatitudes, such as baroclinic disturbances or extratropical Rossby wave trains that could help organize MJO convection (e.g. Kiladis and Weickmann 1992).

The impacts of the Madden-Julian oscillation are extensive, with influences on global weather and climate patterns. Zhang (2013) has summarized our current knowledge of these influences including, but not limited to, Asian summer monsoon precipitation, tropical cyclone activity in the Pacific and Atlantic Oceans, and midlatitude weather patterns. The MJO is linked to an increase in frequency and intensity of winter precipitation along the west coast of the United States.

There is evidence that the MJO can influence the El Niño-Southern Oscillation (ENSO), contributing to the development of El Niño and La Niña conditions. The opposite is true as well, in that ENSO can impact the MJO. ENSO is a coupled ocean-atmosphere oscillation in the Pacific Ocean basin, characterized by anomalous sea surface temperatures (SST). The convective phase of the MJO can propagate farther during an El Niño period. During periods of La Niña, SST in the central and eastern Pacific Ocean are below average, with colder temperatures extending farther into the western Pacific. During these conditions, convection can shut off allowing the MJO to speed up sooner. The MJO is generally most active during ENSO neutral years.

Since its discovery in the 1970s, there has been a significant increase in our general understanding of the MJO. Even so, there is still uncertainty in the underlying dynamics of MJO initiation, propagation, and influences on the tropical atmosphere. Numerous studies have provided focused research on the troposphere and air-sea interface. More recent studies suggest that tropical tropopause layer characteristics are also modulated by the Madden-Julian oscillation on an intraseasonal timescale.

Spectral peaks in OLR show the MJO as a wavenumber 1-3 pattern with eastward propagation and a period of roughly 40 days. This signal does not fall along theoretical dispersion curves, suggesting a distinction between equatorial wave modes and the slower, larger-scale MJO (Wheeler and Kiladis 1999). However, the MJO can trigger wave activity and is often associated with convectively-coupled waves. Latent heat processes during deep convection can excite Kelvin waves with slower phase speeds than would be seen in a dry atmosphere (Straub and Kiladis 2002). Warm temperature anomalies in the middle and upper troposphere are accompanied by cold anomalies near the TTL. Enhanced convection tends to

locally cool the tropopause as a hydrostatic adjustment to the induced upward motion below (e.g. Johnson and Kriete 1982; Holloway and Neelin 2007; Paulik and Birner 2012). The Kelvin wave response is seen as a downward phase propagation of alternating temperature and zonal wind anomalies with vertical wavelengths of 4-5 km. Signals are typically seen above 250 hPa, where the stratification of the stratosphere allows waves to vertically propagate. Kiladis et al. (2001, 2005) describe the eastward tilt with height that is characteristic of a wave forced by an eastward moving convective heating source below, such as the Madden-Julian oscillation. Equatorial wave disturbances such as the MJO can also generate a broad spectrum of both eastward and westward propagating higher frequency waves. Vertically propagating gravity waves transport momentum and can lead to a forcing on the mean flow as they dissipate in the stratosphere (Fovell et al. 1992; Alexander and Holton 1997).

The intraseasonal temperature variability in the TTL directly impacts the height of the tropopause. Studies have used the cold point and lapse rate to indicate the vertical movement of the tropopause with time. Madden and Julian noted the upward bulge in tropopause height in association with the deepest convection. Kim and Son (2012) focused on the cold point tropopause (CPT) because of its relevance for dehydration of air entering the stratosphere, and find the intraseasonal variability of the temperature of the CPT to be dominated by Kelvin wave activity and the MJO. Directly above peak convection the cool phase of the Kelvin wave is below the CPT which results in descending CPT heights (Zeng et al. 2012). MJO enhanced deep convection acts to cool the tropopause and raise the LRT height, while suppressed convection acts to warm the tropopause and lower the LRT height. Intraseasonal equatorial variations in CPT temperature anomalies are around 1.2 K, with variations in tropopause heights generally less than 200 m (Tian et al. 2012).

Previous studies have linked the occurrence of tropopause-level cirrus clouds to both Kelvin wave activity (Boehm and Verlinde 2000) and the Madden-Julian oscillation (Virts and Wallace 2010). Del Genio et al. (2012) describes the typical cloud structure in relation to MJO phase, with cirrus clouds leading peak convection by 10-15 days. High clouds form in situ due to cold temperatures or by detrainment from deep convection and can extend into the lower stratosphere. There is a typically a higher abundance of cirrus clouds over the western Pacific Ocean where tropopause temperature are coldest, compared to the Indian Ocean. The occurrence of TTL cirrus in relation to phases of the MJO show the signature of equatorially trapped Kelvin waves, particularly at levels above 15 km (Virts and Wallace 2010, 2013). At the 100 hPa level, greater cirrus cloud frequency is observed approximately 30°- 45° longitude to the east of MJO-enhanced convection. This pattern is consistent with the descending upper level cool anomalies and higher tropopause heights that precede the active phase of the MJO, which allows water vapor to condense and thin ice clouds to form. As such, the Kelvin wave cold phase is typically followed by anomalously low water vapor concentrations.

MJO-enhanced deep convection and the occurrence of cirrus clouds has radiative impacts on the TTL. Yang et al. (2010) describe the typical net cloud radiative heating from tropopause-level cirrus as strongest near 15 km, with infrared cooling in the cloud-free air above. In boreal winter, the maximum net cloud radiative heating is located over the western Pacific warm pool. During the MJO active phase, cirrus clouds often reside above optically thicker convective clouds so that the TTL is cooled. In general it is expected that the increase in overshooting convection associated with the MJO and the lowering of the level of zero net radiative heating due to infrared heating by cirrus clouds would act to enhance vertical transport. Jiang et al. (2011) found that the MJO signals in radiative heating were

stronger over the Indian Ocean compared to the western pacific. Local infrared heating by tropopause-level cirrus lags peak convection, and shows a westward tilt with height. Johnson et al. (2014) suggest an undersampling of cirrus clouds by ground-based instrumentation during DYNAMO, so that the full radiative effects are not seen.

1.3. The 2011-12 DYNAMO field campaign

To attempt to better understand these processes, a field campaign was specifically designed to study the MJO. Dynamics of the Madden-Julian Oscillation (DYNAMO) became the U.S. component of the international field campaign under the Cooperative Indian Ocean Experiment on Intraseasonal Variability in Year 2011 (CINDY2011). The Atmospheric Radiation Measurement (ARM) MJO Investigation Experiment (AMIE) was an extension of the field campaign that maintained twin observational facilities at Gan and Manus Islands to track the development of the MJO. For simplicity, the term DYNAMO will be used in reference to the cumulative field campaign. The goal of DYNAMO was to collect in situ observations in the Indian Ocean to advance our understanding of MJO convective initiation and propagation, including air-sea interaction. New theories might then be used in order to improve MJO simulations in numerical models with poor representation of MJO variability, and increase predictability. Yoneyama et al. (2013) summarizes the DYNAMO field campaign experimental design and operation.

The observation network consisted of two quadrilateral sounding arrays centered around the region of MJO initiation in the equatorial Indian Ocean, with a broader sounding network extending from Africa to the Maritime Continent. Figure 1.4 indicates the site locations, which were a combination of land and ship sites. In this study, we focus on the twin island sites operated by AMIE, marked by blue diamonds in the figure. Gan Island is

14

located in the equatorial Indian Ocean, while Manus Island is located to the east in the equatorial western Pacific Ocean. This configuration makes it possible to study the same MJO event in its initiation and mature stages while it is still convectively coupled. In addition to radiosondes and surface meteorology instrumentation, multiple radars of different wavelengths provided information on the vertical distribution of clouds and their properties. With the high sampling frequency and fine vertical resolution DYNAMO offers a unique dataset to study the Madden-Julian oscillation.
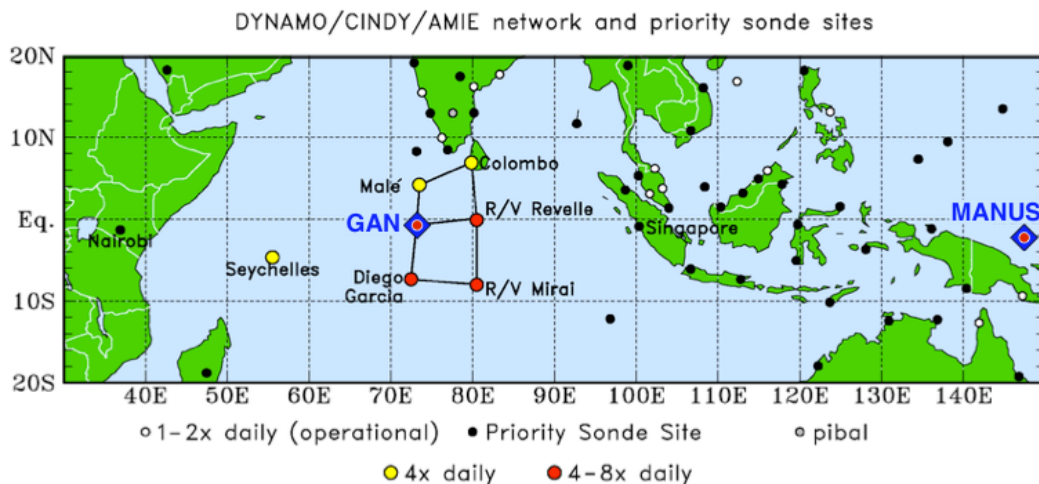
FIGURE 1.4. DYNAMO sounding network spanning the Indian Ocean and western Pacific Ocean. The two sites used in this study are indicated by blue diamonds. Adapted from Johnson and Ciesielski (2013).

The time period for the campaign was based on known climatology of the MJO, with a higher occurrence of initiation during boreal winter. The extended observing period took place from 1 October 2011 to 31 March 2012, with an intensive observing period during the first three months. In general, conditions in the Indian Ocean were favorable for convective development. During the field campaign, three large-scale convective events were observed throughout the October to December time period. The first occurred in late October and the second occurred in late November, roughly 30 days later. These were clearly associated with

the MJO, showing strong convective initiation in the tropical Indian Ocean and eastward propagation. A third convective event was seen in late December. This was considered to be a weak MJO-like event in that it showed MJO characteristics, but did not fit the conventional definition and so will not be considered in this study. Focus will be on the two prominent MJO active phases in October and November.

To put these two in context of MJO observations from previous campaigns and model simulations, it is beneficial to consider the general atmospheric and oceanic conditions during DYNAMO. Local (70-80E) upwelling of the of the Brewer-Dobson circulation over the DYNAMO sounding array was anomalously strong in comparison to the October climatology. The cold phase of the El Niño-Southern Oscillation was present throughout the entirety of the campaign. MJO strength is coupled to ENSO. In this case, the La Niña conditions during the DYNAMO time period meant that the central Pacific Ocean sea surface temperatures were cooler than average, likely causing the MJO events to decouple from convection and speed up sooner. Further discussion of the background state of ENSO, the Indian Ocean dipole, and monsoon circulations can be found in Gottshalck et al. (2013).

There were notable differences between the October and November MJOs, as discussed by Johnson and Ciesielski (2013). The October MJO had more convection, with signals showing 2 day waves. However, the November MJO could be considered to be the stronger MJO event. Two prominent Kelvin waves in the troposphere were associated with deeper convection, greater peak precipitation, and stronger low-level westerlies than was seen for the October MJO. Some of these features can be seen in Figure 1.5, which shows rainfall over the DYNAMO sounding network during October to December 2011 from TRMM data.
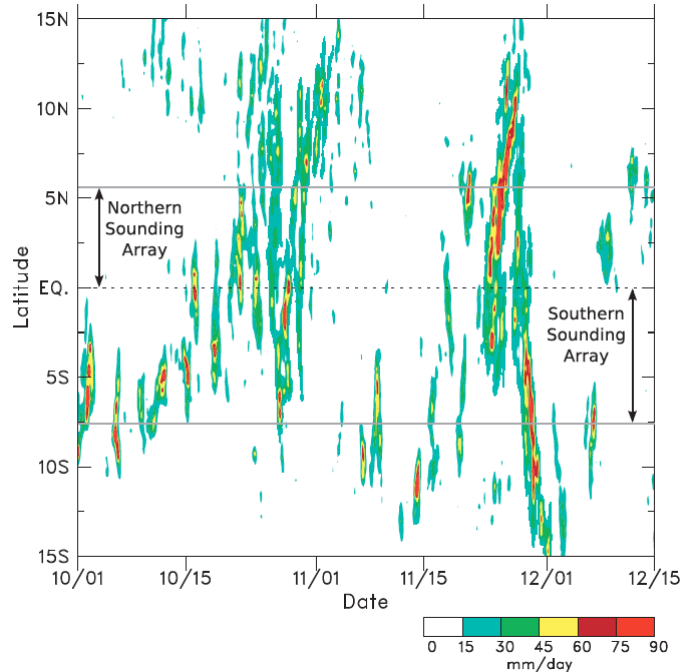
FIGURE 1.5. Time-latitude diagram showing TRMM precipitation averaged 72°E-80°E during the DYNAMO field campaign. From Johnson and Ciesielski (2013).

1.4. RESEARCH OBJECTIVES

The overlying idea and motivation behind this work is to increase our understanding of the major drivers of stratospheric water vapor concentration, and the processes that lead to changes on different timescales. One phenomenon that is thought to influence changes in stratospheric water vapor is the Madden-Julian oscillation. We expect to see a change in tropical tropopause layer properties as a response to the increase in deep convection associated with the MJO. It is known that the MJO increases the frequency of overshooting convection, which will have a direct impact on vertical transport. Furthermore, cirrus cloud formation plays an important role in the dehydration of the TTL and is thought to be modulated by the MJO indirectly through cooling by equatorial waves.

Previous studies, such as those by Virts and Wallace (2010, 2014), have looked at relationships between the MJO and the TTL from a general perspective, and have made strides in our understanding. This work takes a case study approach, using high resolution data from the DYNAMO field campaign to focus on individual MJO active periods. The goal of this study is to better understand the extent to which the tropical tropopause layer is modulated by Madden-Julian oscillation dynamics at the equator. In doing so, we hope to address the following questions: 1. How does the MJO impact temperature variability in the TTL and how might this affect stratospheric water vapor? 2. How does modulation by the MJO compare to TTL variability on different timescales? 3. Is the TTL response dependent on the location/phase of the MJO?

This manuscript is organized as follows. Chapter 2 describes the data sets and analysis techniques used in this study. Chapter 3 gives an overview on the background conditions of the two sites analyzed, Gan Island and Manus Island. Wave activity and the multiscale variability in the TTL will be addressed in Chapter 4, while tropopause-level clouds and their impact on radiative heating will be discussed in Chapter 5. Chapter 6 summarizes the major findings of this study and offers suggestions for future work.

CHAPTER 2

Data and analysis techniques

2.1. Data sources

2.1.1. DYNAMO atmospheric soundings. The primary dataset used in this study is from the 2011-12 Dynamics of the Madden-Julian Oscillation (DYNAMO) field campaign. DYNAMO consisted of a broad sounding network providing high resolution observational data for multiple sites, as marked in Figure 1.4. Here we have focused on two core sites. Gan Island, Republic of the Maldives ($0.7°S$, $73.2°E$) is located in the central-equatorial Indian Ocean, in the region of MJO initiation. The MJO will continue to develop during its eastward propagation into the western Pacific Ocean where our comparison site, Manus Island, Papua New Guinea ($2.1°S$, $147.4°E$), is located.

At each location, Vaisala RS92 radiosondes were launched every three hours beginning at 00 UTC. Data for Gan are available for the 1 October 2011 through 31 December 2011 time period, while data for Manus extend through 31 March 2012. Observations were provided at 50-meter vertical resolution, including measurements of atmospheric pressure, wind velocity, air temperature, and dew point. The high spatial and temporal resolution at these sites is an advantage of the field campaign, and allows us to analyze small-scale features that may otherwise have been missed.

A disadvantage of the dataset is that the vertical extent of radiosonde observations is limited to the height the balloon reaches before bursting. In a small percentage of cases this happened before reaching the tropical tropopause layer, likely due to icing on the balloon. This was more frequent during deep convective time periods, particularly during active phase of the MJO. The distribution of the highest heights reached (bursting level) for Gan and

Manus are shown in Figure 2.1. For upper-level analysis that required continuous data, a cubic spline interpolation was used to approximate the few missing data points. It should also be noted that while humidity has been used for analysis in Chapter 5, it is known that the radiosondes exhibit a daytime dry bias that had to be corrected for. Upper-level humidity measurements in particular should be used with caution, as they tend to be on the dry side when compared to operational model data counterparts. Further discussion of DYNAMO sounding data and quality control procedures can be found in Ciesielski et al. (2014).
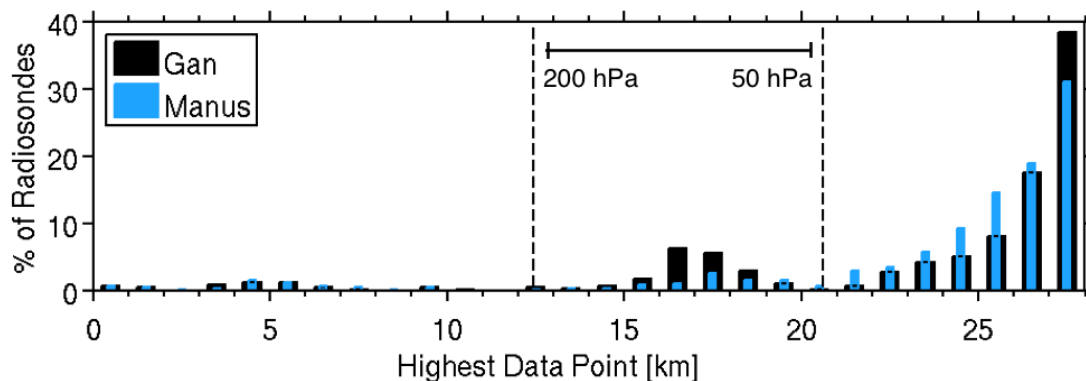
FIGURE 2.1. Distribution of the highest data points available from DYNAMO atmospheric soundings throughout the 1 October to 31 December 2011 time period. The percentage of radiosondes that reach each height are relative to a total of 745 radiosondes launched at Gan Island (black) and a total of 670 radiosondes launched at Manus Island (blue). The 50-200 hPa region is indicated as a reference for the tropical tropopause layer.

The latest version of DYNAMO gridded datasets can be accessed at http://johnson.atmos. colostate.edu/dynamo/products/gridded/.

2.1.2. PNNL COMBINED RETRIEVALS. The Atmospheric Radiation Measurement (ARM) MJO Investigation Experiment (AMIE) took place in conjunction with the DYNAMO field campaign and provided additional data. Gan Island was chosen as a "radar supersite" with

multiple radars of different wavelengths providing relevant information on the vertical distribution of clouds and their properties. The K_a-band ARM Zenith Radar (KAZR) is a Doppler cloud radar operated at a K_a-band (8.6 mm wavelength). The data product tops at just below 18 km in altitude, with a minimum detectable reflectivity estimated at -40 dBZ. KAZR is known to underestimate cloud top height due to attenuation during heavy precipitation (Feng et al. 2014). This becomes important when interested in high clouds, such as cirrus. The S-band Polarization Radar (S-Pol) is dual-polarimetric radar operated at an S-band (10 cm wavelength). The Shared Mobile Atmospheric Research and Teaching Radar (SMART-R) is a scanning single-polarimetric Doppler radar operated at a C-band (5 cm wavelength).

Data collected during AMIE was incorporated into a Pacific Northwest National Laboratory (PNNL) product, which uses a Combined Remote Sensor retrieval algorithm (CombRet) for cloud and precipitation properties. Broadband radiative flux and heating rate profiles are calculated using a radiative transfer model that inputs atmospheric profiles from these observations. Data are provided on 224 vertical levels, with 30-second time resolution during the 11 October 2011 to 7 February 2012 time period. In this study, we are interested in how tropopause-level cirrus clouds might be associated with changes in the radiative heating rate profile. Radar reflectivity and shortwave/longwave heating rates from the PNNL product are analyzed in Chapter 5, although the product is only available for Gan and not Manus.

For more on AMIE experimental design and data collected, see Yoneyama et al. (2013) and Feng et al. (2014). The latest version of PNNL combined retrievals, microphysical retrievals, and heating rates are available through the ARM Data Archive at http://www.arm.gov/data/pi/71.

2.1.3. CALIPSO. In an effort to study the effects of cirrus clouds on radiative heating rates, it was determined early on that ground-based radar on Gan Island were not able to detect tropopause-level clouds. As a result Cloud-Aerosol Lidar and Infrared Pathfinder Satellite Observations (CALIPSO) satellite data has been used as a supplement. The main instrument is the Cloud-Aerosol Lidar with Orthogonal Polarization (CALIOP), which operates at wavelengths in the visible (532 nm) and near-infrared (1064 nm) part of the spectrum. It provides high-resolution vertical profiles of attenuated backscatter by aerosols and clouds, as well as information on their properties.

CALIPSO has a Sun-synchronous orbit, with a period of 99 minutes and a repeat cycle every 16 days. An overpass at the equator occurs twice daily around 0130 and 1330 local time. Based on the infrequency of a direct overpass of a single site, any CALIPSO data that fell within a 10°x10° latitude-longitude box centered around Gan Island or Manus Island was considered. The short time series associated with each overpass was temporally averaged to create a single profile. Data used for analysis are from the 1 October 2011 to 31 December 2011 timeframe, with a period of missing data seen during late November at Gan Island.

The cloud layer fraction parameter is provided in the level 2, 5 km Lidar Cloud Profile Data product. This fraction is based on the detection of cloud within a 5 km (horizontal) by 60 m (vertical) cloud profile range bin. Lidar is able to detect optical depths as small as 0.01, but quickly attenuates beyond optical depths of 3 (Winker et al. 2007). This means that it is capable of detecting high cirrus clouds, though cloud layers near the surface may not be captured in the presence of deep convection. In this study, the indication of tropopause-level cirrus during an overpass is based on the presence or lack of a thin cloud band near the 100 hPa level, distinct from lower level convection.

More information on CALIPSO and the instrumentation onboard can be found through the NASA website, http://www.nasa.gov/mission_pages/calipso/main/index.html. Data are available through the NASA Langley Research Center Atmospheric Science Data Center (ASDC) at https://eosweb.larc.nasa.gov/.

2.1.4. ECMWF OPERATIONAL ANALYSIS AND ERA-INTERIM. In addition to observational data taken during the DYNAMO field campaign, model data was used as a comparison. Model data has the benefit of being available for a range of longitudes, providing information on the horizontal scale of atmospheric waves that is not possible with site measurements. Two data products from the European Centre for Medium-Range Weather Forecasts (ECMWF) are used in this study. ECMWF operational model analysis was considered over the 1 October 2011 to 31 December 2012 time period, in correspondence with the DYANMO field campaign. The gridded data interpolated to Gan Island was provided on 91 hybrid levels, with 19 pressure levels between 50-200 hPa. The second product, ECMWF Re-Analysis (ERA)-Interim, was considered over an extended time period, 1 August 2011 to 29 February 2012. Gridded data was taken at the equator with a 0.7° longitude resolution, and had 60 model levels with 9 pressure levels between 50-200 hPa.

Model levels are converted to pressure levels following $p = a + b(p_s)$, where a and b are coefficients given as a function of model level and p_s is the surface pressure, dependent on time and space. For both ECMWF products time resolution is 6-hourly starting at 00 UTC. Basic fields analyzed include pressure, temperature, winds, and radiative heating rates.

ECMWF operational analysis data are available with permission through the NCAR Research Data Archive (RDA) at http://rda.ucar.edu/datasets/ds113.0/. More information and ERA-Interim data are available through the ECMWF website at http://apps.ecmwf.int/datasets/.

2.2. Analysis techniques

2.2.1. Madden-Julian oscillation index. The best method for identifying the Madden-Julian oscillation is an ongoing discussion in the field. In this study the time-varying phase of the MJO is determined using the index developed by Wheeler and Hendon (2004), see Figure 2.2. The diagram shows the relative strength and location of the MJO active phase during its eastward propagation (counter-clockwise) around the globe. This Real-time Multivariate MJO (RMM) index is based on the first two empirical orthogonal functions (EOFs) of 200 hPa zonal wind, 850 hPa zonal wind, and outgoing longwave radiation (OLR) averaged from $15°N - 15°S$.
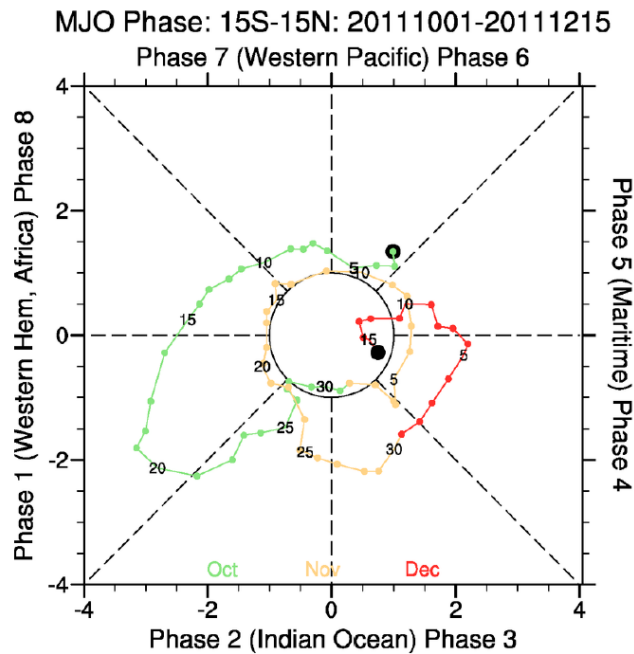

FIGURE 2.2. RMM index for the 1 October to 15 December 2011 time period, where counter-clockwise describes eastward motion. Data points reflect the phase and relative strength of the MJO for each date. From Johnson and Ciesielski (2013).

As Gan Island is located in the central Indian Ocean, dates corresponding to RMM phases two and three are used as a general timeframe for an MJO active phase at that site. Two prominent MJO active phases are indicated during the DYNAMO field campaign, 21 October to 4 November and 22 November to 2 December. A weak MJO signal is also indicated in late December (not shown), but is of smaller scale and faster propagation so will not be considered in this study. The two MJO active phases are seen at Manus Island in the days following as indicated by RMM phases five and six, 7-11 November and 6-11 December.

Recent studies suggest new methods for identifying the active phase of the MJO, including a velocity potential multivariate MJO index (VPM; Ventrice et al. 2013) and an OLR-based MJO Index (OMI; Kiladis et al. 2014). These indices put emphasis on different characteristics of the MJO as a way to define the active phase. The overall MJO features are similar for all indices, with the timing shifted by a few days at most. If the convective signal associated with the MJO was the predominant interest for example, a solely OLR-based index may be more appropriate. In this study however, a precise definition of the MJO active phase is not important. The RMM index has been the standard, and serves our purpose as a general indicator of the passage of an MJO active phase over the Indian Ocean and western Pacific.

2.2.2. COLD POINT AND LAPSE RATE TROPOPAUSE. Thermal tropopause measures are discussed in Section 4.1. The cold point tropopause is determined by the coldest pressure level between the troposphere and stratosphere in a temperature vertical profile. In this case, 3-hourly DYNAMO temperature data were daily-averaged to account for missing data at upper levels and smooth out small scale disturbances. The lapse rate tropopause was calculated as defined by the World Meteorological Organization: "the lowest level at which

the lapse rate decreases to 2 K km^{-1} or less, provided that the average lapse rate between this level and all higher levels within 2 km does not exceed 2 K km^{-1}." In practice this means starting from the lowest level in the temperature profile and finding the point where the lapse rate reaches 2 K km^{-1}. From that level, each increasing increment up to 2 km is then checked for a lapse rate greater than 2 K km^{-1}. If such a lapse rate is found, the process starts at the next highest level and repeats until the conditions are met.

2.2.3. SPECTRAL ANALYSIS. In Section 4.2, spectral analysis is used to investigate the multiscale variability in the TTL using data from DYNAMO atmospheric soundings. The idea is that spectral peaks could reveal the presence of equatorial waves that are associated with a range of frequencies. The units of power are converted to a fraction of variance by squaring, and then normalized by dividing by the sum over all frequencies. In testing the statistical significance of the peaks, the null hypothesis was that features in the power spectra could be explained by background red noise. In other words, that power density decreases with increasing frequency due to persistence in the data. A theoretical red noise spectrum was fit to each temperature and wind power spectrum using a lag-one autocorrelation of the original time series, and then scaled to have the same variance as the original time series power spectrum. The F-statistic could then be used to test the significance of the ratio of the two variances. The number of degrees of freedom $\nu = 16$, was assumed based on the averaging 8 adjacent spectral estimates together and 2 degrees of freedom per spectral estimate.

Prior to applying a Fourier transform the seasonal trend was removed using a linear fit. Since DYNAMO atmospheric soundings are limited to a 92 day period, a Hann window was applied to reduce the introduction of peaks in the spectra due to finite windowing and the short time frame. A priori statistics have been used since we have reason to expect

peaks related to the MJO and atmospheric waves. For comparison the analysis was repeated using ERA-Interim data over the full 1 August 2011 to 29 February 2012 time period. The additional two months on either end provide a longer interval to find periodicity in the data.

2.2.4. TEMPORAL FILTERING. A Butterworth filter was used to separate out temperature and wind anomalies associated with equatorial waves on different time scales. The data were filtered in three ways. Bandpass filtering for a frequency band corresponding to periods of 20-80 days was used isolate low frequency signals, such as the Madden-Julian oscillation. Bandpass filtering for a frequency band corresponding to periods of 7-20 days was used to isolate mid-range frequency signals, such as Kelvin waves (Wheeler and Kiladis 1999; Fujiwara et al. 2012). Highpass filtering for frequencies corresponding to periods less than 7 days was used to isolate higher frequency waves, such as gravity waves. For DYNAMO atmospheric soundings filtering is based on a sampling frequency of 8 day^{-1}, while for ERA-Interim filtering is based on a sampling frequency of 4 day^{-1}. Prior to filtering, a Hann window was applied to each time series so that middle points are weighted most heavily and the edges are tapered. This minimizes issues related to boxcar windowing, such as aliasing and spectral leakage in our short time domain.

The Butterworth filter is designed to have as flat a passband as possible. It is a recursive filter in that it uses previous data and can be done in real time. However, this means that with the initial spin-up, data at the beginning of the time series should not be trusted. Figure 2.3 shows the impulse response function for each bandpass and highpass filter used. The output is associated with the memory in the function from a brief input signal, and shows that the lower the frequencies filtered, the longer the spin-up time required. For instance, after 10 days the 7 day highpass response is near-zero, while the 20-80 day bandpass takes at least 20 days to adjust. Filtering was done in both the forwards and backwards direction to

correct for phase shifts in the data, and data at both the beginning and end of the time series are compromised. Although DYNAMO data from 1 October to 31 December 2011 was used in filtering, only dates between 11 October to 15 December 2011 are shown in the analysis. This adjustment period is less of an issue for ERA-Interim data since a longer time series is available, and we are able to disregard early or subsequent data that does not overlap with the DYNAMO field campaign.
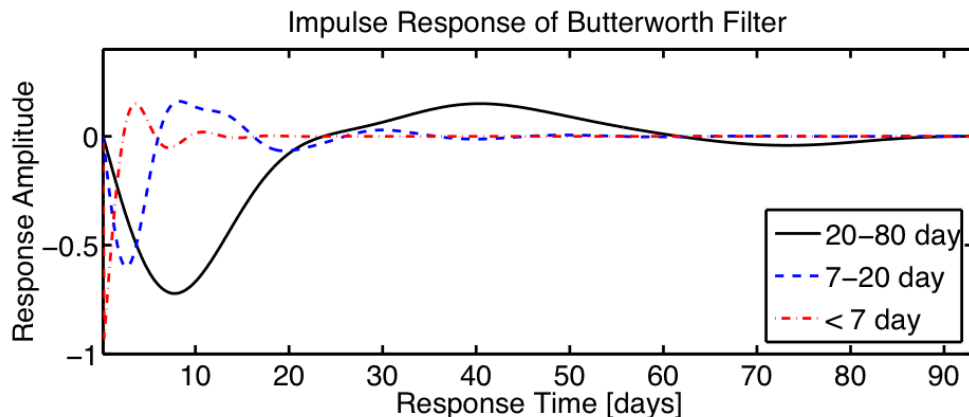
FIGURE 2.3. Impulse response function for a Butterworth filter with a 20-80 day bandpass, 7-20 day bandpass, and 7 day highpass.

2.2.5. LOWER STRATOSPHERIC WAVE ANALYSIS. The lower stratospheric wave analysis in Section 4.3 follows a similar method to those used in studies such as Allen and Vincent (1995) and Wang and Geller (2003). At each timestep, individual sounding profiles of temperature and horizontal winds could be compared to their second-order polynomial fits of the form $y = ax^2 + bx + c$, see Figure 2.4. The quadratic fit is used to represent a background mean profile. The difference between the sounding profile and the mean profile would give an anomaly in space rather than time which will be denoted with an asterisk hereafter, $T^* = T - T_{fit}$. To calculate variance, the anomaly at each pressure level is then squared before taking the 30-85 hPa layer vertical mean.

The variance in wind is proportional to kinetic energy density as follows,

$$(2.1) \qquad K_e = \frac{1}{2}\left[\overline{u^{*2}} + \overline{v^{*2}}\right].$$

Similarly, the variance in temperature is proportional to potential energy density,

$$(2.2) \qquad P_e = \frac{1}{2}\frac{g^2}{\langle N^2 \rangle}\frac{\overline{T^{*2}}}{\overline{T}^2}$$

where $\langle N^2 \rangle = \left\langle \frac{g}{T}\left(\frac{\partial T}{\partial z} + \frac{g}{c_p}\right)\right\rangle$ is the squared buoyancy frequency, $g = 9.8\ m\ s^{-1}$ is the gravitational constant, and $c_p = 1004\ J\ kg^{-1}\ K^{-1}$ is the specific heat of dry air at constant pressure. In these equations, asterisks indicate an anomaly with respect to a quadratic fit, while overbars and angle brackets denote a vertical mean was taken.
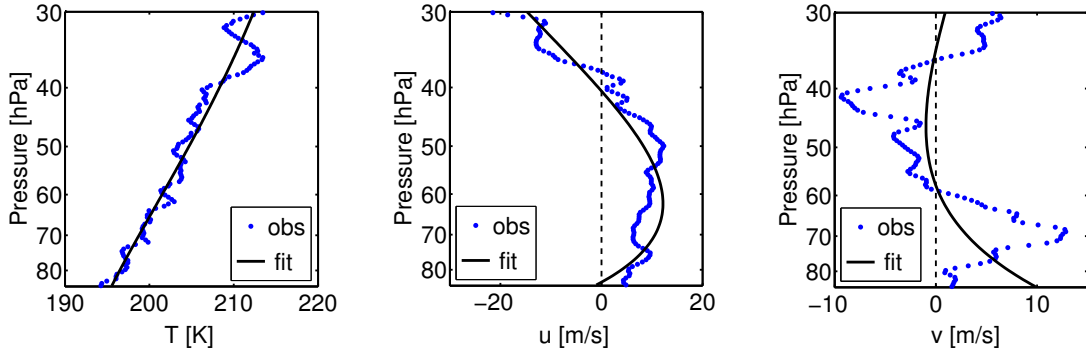
FIGURE 2.4. Vertical profiles of lower stratospheric temperature, zonal wind, and meridional wind from a DYNAMO atmospheric sounding on 10 November 2011 at Gan Island. The corresponding second-order polynomial fits for the 30-85 hPa layer are shown in black.

The 30-85 hPa layer was chosen with a lower boundary above the cold point tropopause and upper boundary limited by data availability, see Figure 2.1. In the tropics the 30-85 hPa layer is roughly 6.2 km deep. For waves with a vertical wavelength that do not fit nicely into this domain, a quadratic fit may not be representative of the background structure. The method worked well for Wang and Geller (2003) in studying gravity waves. However, in this study larger scale Kelvin waves are present and the quadratic fit method led to dubious results. One way around this was to filter the data in order to take out the background

vertical structure and leave only the anomalies associated with atmospheric waves. The variance was still taken over the vertical layer in order to calculate the wave energy, but without first subtracting a quadratic fit. This modified method is only used with 7 day highpass and 7-20 day bandpass filtering, as we would not expect to see a 20-80 day signal associated with the MJO in the lower stratosphere. In the calculation for potential energy where a reference temperature profile is needed ($\overline{T}^2$, $\frac{\partial T}{\partial z}$), the October to December time mean is used.

2.2.6. RELATIVE HUMIDITY. Relative humidity (RH) is a measure of water vapor in the atmosphere. Put simply, it is the amount of moisture in the air compared to the amount of moisture there could be in that air needed to reach saturation at a specific temperature. Once saturation is reached, water vapor has the potential to condense into the liquid phase and form clouds. RH has been calculated starting with the formula for saturation vapor pressure in Garand et al. (1992),

$$(2.3) \qquad\qquad e_s = 6.1078 \; exp[a(T - 273.16)/(T - b)]$$

where e_s is the saturation vapor pressure in milibars, T is the temperature in Kelvin, and a and b are coefficients. For the ice phase $a_i = 21.875$ and $b_i = 7.66$ K, while water phase values are $a_w = 17.269$ and $b_w = 35.86$ K. The equation is used twice, as a function of both the dew point (T_d) and the ambient temperature (T_a). RH is then calculated from the ratio of vapor pressures,

$$(2.4) \qquad\qquad RH = \frac{e_s(T_d)}{e_s(T_a)} \; \times \; 100\%.$$

In the TTL, where temperatures are below freezing, the RH has been calculated with respect to ice using the ice phase constants a_i and b_i. RH over 100% are possible due to supersaturation, when environmental conditions are such that air contains more water vapor than is needed for saturation. RH was chosen to quantify TTL moisture in Chapter

5 since temperature and dew point are directly available from the DYNAMO atmospheric soundings, keeping in mind that upper level water vapor concentrations are small and so instrumentation measurements may not be reliable.

2.2.7. RADIATIVE HEATING RATES. Broadband shortwave and longwave heating rate profiles were used from the PNNL and ERA-Interim data products. To find the total broadband heating rates, the sum of shortwave and longwave heating rates were calculated. Cloud radiative forcing was calculated by subtracting clear-sky data from full-sky data. The level of zero net radiative heating (LZRH) is the level at which a radiative heating profile crosses from radiative cooling (below) to radiative heating (above) in the tropics.

CHAPTER 3

Background conditions of Gan and Manus Islands

In this study we analyze Madden-Julian oscillation observations at two sites, Gan Island in the central Indian Ocean and Manus Island in the western Pacific Ocean. With Africa to the west, Asia to the north, and the Maritime Continent to the east, the Indian Ocean is unique in that it is bounded by land mass on three sides. It is in this region that MJO initiation takes place. Organized MJO convection will generally start over the Indian Ocean and propagate eastward toward the Pacific Ocean.

Different features can often be found at Manus Island due to its proximity to the west Pacific warm pool. Compared to Gan Island, this site is located in a region of warmer sea surface temperatures, a result of the equatorial trade winds blowing warm surface water westward in the tropical Pacific Ocean and causing an upwelling of cool water to the east. The warm pool oscillates on seasonal and interannual timescales such as the El Niño-Southern Oscillation with shifts in position, average temperature, and sea level pressure due to the Intertropical Convergence Zone (ITCZ) and the zonal-vertical Walker Circulation in the Pacific Ocean. In addition to warmer temperatures, the west Pacific warm pool is associated with lower sea level pressure, intense convection and rainfall, and on average, colder and higher tropopause heights (see Figure 1.2).

Figure 3.1 shows the October to December 2011 mean geopotential heights, winds, and temperature anomalies at the 95 hPa level using ERA-Interim data. This time period is in the transition between July and January seasonal extremes, shown earlier. During DYNAMO, the geopotential height anomaly field and associated winds show a spatial pattern that is influenced by the symmetric Rossby gyres characteristic of boreal winter. The distribution of temperature, with a pocket of colder tropopause temperatures shifted to the north and west over southeast Asia, more closely resembles that of boreal summer.
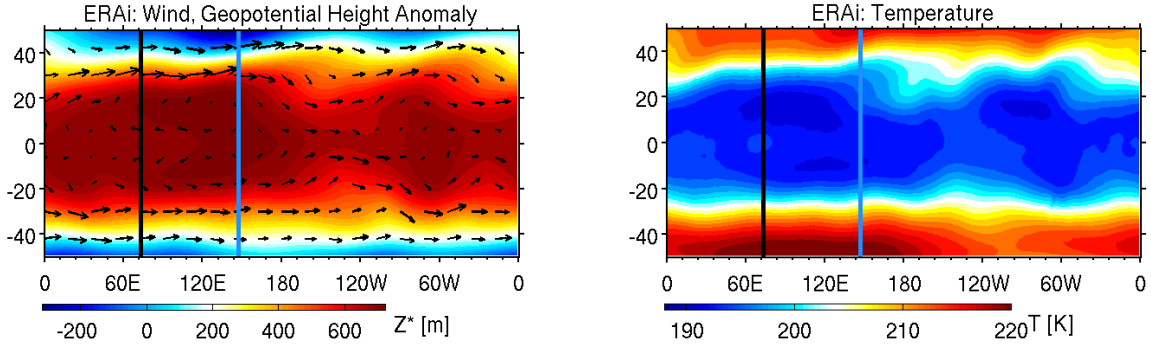
FIGURE 3.1. 95 hPa maps of October-December 2011 mean fields for [left] wind (vector field) and geopotential height anomaly and [right] temperature, from ERA-Interim model data. For reference, solid vertical lines mark the longitude of Gan Island (black) and Manus Island (blue).

Locally, wind and temperature features can change on shorter timescales. Figure 3.2 shows unfiltered zonal wind velocity in the upper troposphere and lower stratosphere at Gan and Manus Island from October-December. In the lower stratosphere the tropical zonal wind direction reflects the westerly phase of the stratospheric quasi-biennial oscillation at the time of DYNAMO. The strong descending easterly wind seen near 30 hPa toward the end of the time period signals the onset of the easterly phase of the QBO at higher levels. A sharp vertical gradient near 100 hPa marks the transition from westerlies above to prevailing easterlies in the layer below. The background mean flow is critical for the vertical propagation of waves in the atmosphere. Equatorial wave theory dictates that eastward-propagating Kelvin waves require a background easterly flow, or weak westerly flow (Flannaghan and Fueglistaler 2013).

In comparing the two island sites, Gan has stronger easterlies in the upper troposphere. At Manus Island, there are periods below 100 hPa that have notable westerlies, including mid-October, early November, and late November. This resembles the MJO anomalous circulation seen in Figure 1.3, with upper-level westerlies preceding the MJO. These features are not seen at Gan and may be attributed to differences in regional climatology between the two sites. Higher sea surface temperatures and frequent tropical convection at Manus may contribute to anomalous flow unrelated to the MJO. It is also possible that in October

FIGURE 3.2. Time series of unfiltered zonal wind in the TTL at (a) Gan Island and (b) Manus Island, from DYNAMO observations. Positive (negative) values represent westerly (easterly) winds.

Gan is still influenced by the large-scale Tibetan anticyclone seen in the boreal summer months, while Manus is further away and modulated by smaller subtropical circulations. Both locations show distinct descending anomalous wind patterns indicative of equatorial Kelvin waves, discussed further in Chapter 4. One example of this is the 10-day time period from 21-31 October at Gan, in which a strong maximum in westerlies show a descending pattern from 40 to 100 hPa.

Meridional winds are shown for the month of October at Gan Island in Figure 3.3. Though only shown for Gan, similar scale features are seen in the Manus Island data, as well as throughout the months of November and December. The tilted structures associated with the northerly and southerly winds are of smaller scale and are more prevalent than seen in the zonal wind. Larger-scale Kelvin wave anomalies are not expected to show up in the meridional wind field, which means that wave activity must be dominated by a combination of higher frequency gravity waves, Rossby waves, and mixed Rossby-gravity waves. As with

zonal wind, the greatest wave activity in meridional wind is above the 100 hPa level, where the atmosphere is stably stratified. The difference in wave structure and scale between zonal and meridional winds suggests there is a broad spectrum of atmospheric waves in the TTL during DYNAMO.

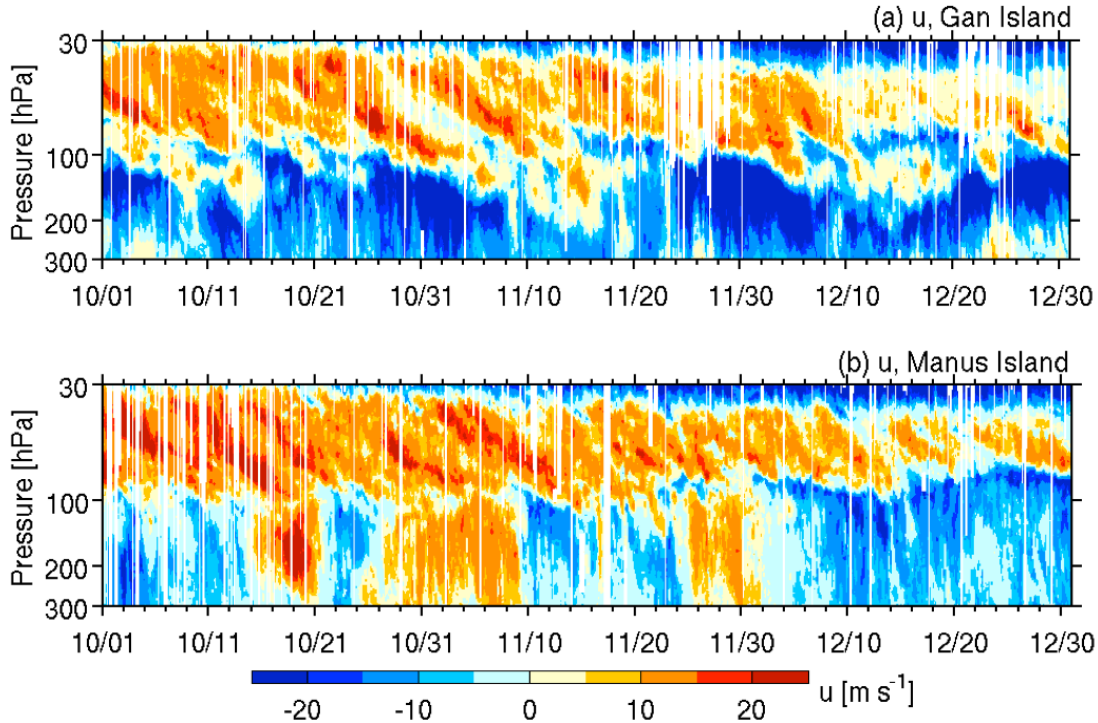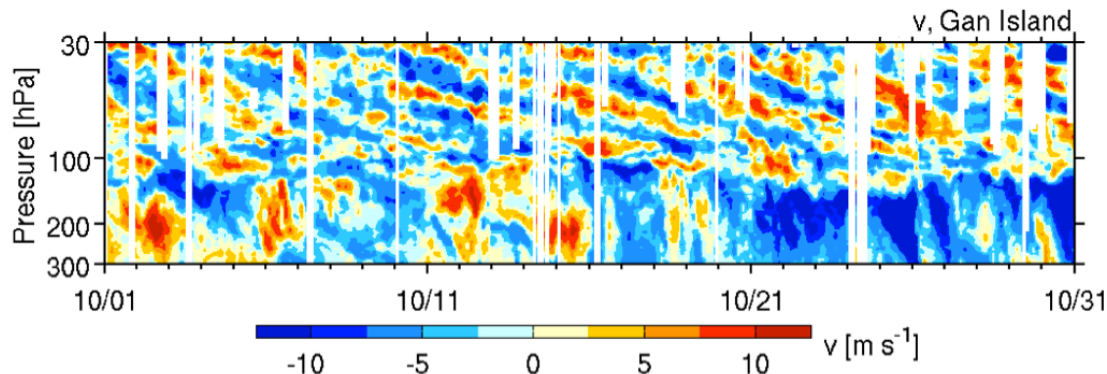
FIGURE 3.3. Time series of unfiltered meridional wind in the TTL at Gan Island, from DYNAMO observations. Positive (negative) values represent southerly (northerly) winds.

In the wave analyses, anomalies are found using mean profiles as a background state for comparison. Figure 3.4 shows the mean vertical profiles of tropical tropopause layer characteristics during the 1 October to 31 December time period, as well as individual monthly averages to back out the seasonal trend. Gan (black) and Manus Island (blue) profiles are plotted together. The background temperature structure has the same shape at both locations, having decreasing temperatures with height in the tropopsphere and increasing temperature with height in the lower stratosphere. The temperature minimum, or cold point tropopause, occurs near 95 hPa. As expected from regional climatology, the cold point tropopause at Manus is slightly colder by roughly 2 K.

The corresponding lapse rate profiles highlight the crossover from a positive to negative change with height due to the temperature inversion in the lower stratosphere. Below this level, the lapse rate is non-linear with a maximum of roughly 8 K km^{-1} at 180 hPa, near the level of main convective outflow. Above 85 hPa the lapse profiles are fairly constant, with temperature increasing at a rate of roughly 4 K km^{-1}. At Manus, the lapse rate is
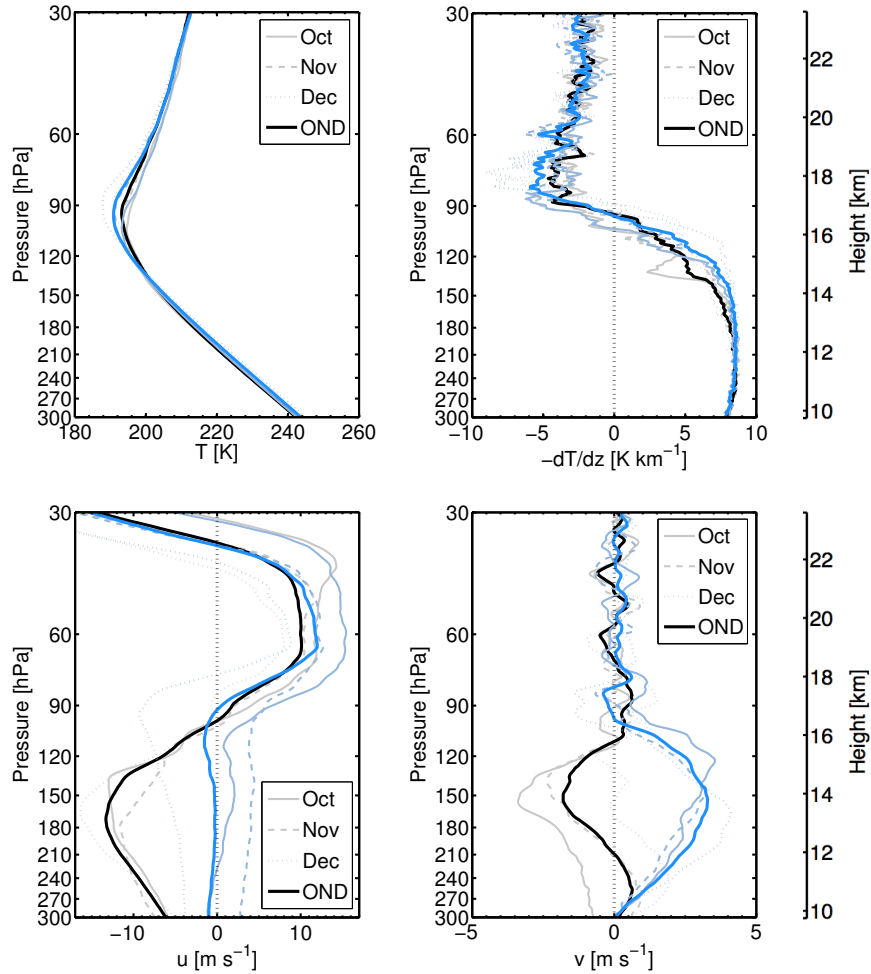
FIGURE 3.4. Mean vertical profiles of TTL properties from 2011 DYNAMO atmospheric sounding data, including temperature, lapse rate, zonal wind, and meridional wind. Solid black and blue lines represent averages over the 1 October to 31 December time period, while lighter colors represent October, November, and December monthly averages. Black/gray profiles denote Gan Island data, while blue/light blue profiles represent Manus Island data. The corresponding height scale is shown here for reference, though atmospheric pressure will be used as the vertical coordinate in subsequent analyses.

slightly more negative at this height, which is likely associated with the west Pacific warm pool. Frequent convection creates cold anomalies near the tropopause, which may also be influenced by a Kelvin wave due to a Matsuno-Gill response to the warmer sea surface temperatures in this region. These temperature and lapse rate profiles can be related to tropopause sharpness, as well as the static stability of the layer (Grise et al. 2010). In the case of Manus Island, static stability is enhanced.

Mean zonal wind profiles are notably different between the two locations, particularly in the upper troposphere. Background zonal wind at Gan peaks with an easterly wind speed of ~13 m s^{-1}, whereas the zonal wind at Manus averages to near zero below 95 hPa (see Figure 3.2). Above this level winds are consistently from the west and directly correspond to QBO phase. In the TTL, the meridional wind component has a smaller magnitude with peak wind speeds near 150 hPa, where outflow is typical, of less than 4 m s^{-1} at either site. The mean profile at Manus shows a northward flow, linked to the poleward branch of the northern hemisphere Hadley cell circulation. This signature is stronger than at Gan Island, which actually shows a mean southward flow, suggesting the role of local precipitation effects and the difference in proximity to the west Pacific warm pool. Meridional wind and wind shear is negligible above 100 hPa at both locations.

A disadvantage to analyzing individual island sites rather than an area average is that local weather can become pronounced in the observations rather than conveying the large-scale aspects of the MJO. This is evident in site specific rainfall time series during the DYNAMO field campaign. Figure 3.5 shows the measured daily precipitation from surface meteorology sites on both Gan (black) and Manus (blue) Island, with shading to indicate the periods that correspond to MJO active phases for each location. At Gan the highest precipitation was seen in mid-October and late November with rates exceeding 40 mm day^{-1}. The timing slightly precedes the MJO active periods defined by the RMM index. This could be an indication that individual squall lines were passing through in addition to MJO convection, leading to the variability seen throughout the period. At Manus Island the maximum precipitation rate is nearly 70 mm day^{-1} on 13 October. Heavy precipitation periods with peaks near 50 mm day^{-1} are also seen in mid-November and late December. As with Gan, the rainfall maxima over the islands of the Maritime Continent do not coincide with the MJO active phases (Peatman et al. 2014). Johnson and Ciesielski (2013) show that precipitation averaged over the DYNAMO northern sounding array in the Indian Ocean does show large-scale features consistent with the MJO passages in October and November.
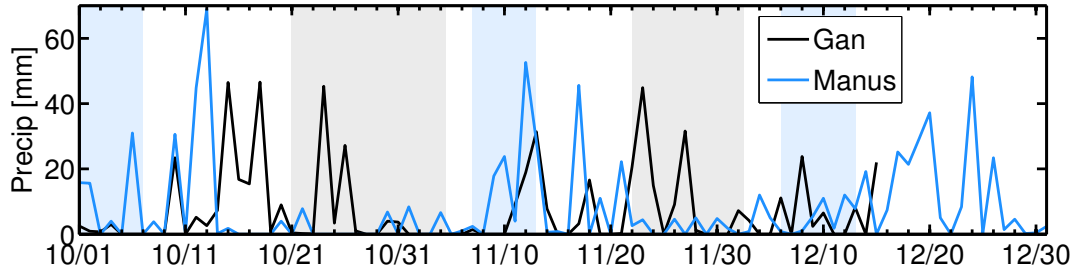
FIGURE 3.5. Time series of daily precipitation using rain gauge data from surface meteorology sites on Gan Island (black) and Manus Island (blue) during the 2011 DYNAMO field campaign. Periods during RMM index phases two and three are shaded gray, corresponding to the active phase of the MJO over the Indian Ocean. Periods during RMM index phases five and six are shaded light blue, corresponding to the active phase of the MJO over parts of the Maritime Continent and western Pacific Ocean. Note: Gan Island data are missing after 15 December.

Radar reflectivity from AMIE ground-based instrumentation on Gan Island shows temporal variability as well, as seen in Figure 3.6. Increased convection and higher cloud top heights are found preceding and during the MJO active phases in late October and late November. Unfiltered TTL temperature anomaly contours are overlaid and show distinctive alternating warm and cool periods associated with equatorial Kelvin waves. The descending cool anomalies above tropospheric deep convection during the MJO active phases are coincident with the higher cloud tops and seem to be prolonged below 100 hPa, particularly for the November MJO. This figure suggests that 1) MJO convection excites wave activity and 2) the depth of convection is modulated by the descending Kelvin waves and may increase overshooting convection, i.e. convection that extends into the TTL. No tropopause-level cirrus clouds are evident in this dataset. However, the K_a-band ARM Zenith Radar (KAZR) was unable to detect these cirrus due to frequent attenuation by rain and limitations in radar sensitivity (Feng et al. 2014). Cirrus cloud occurence in the TTL during DYNAMO will be a further topic of discussion in Chapter 5.

Radar data was only available for this type of analysis for Gan Island. It is likely that MJO convection did not reach Manus with the same intensity that was seen at Gan. This is due in part to the La Niña conditions throughout the DYNAMO field campaign.
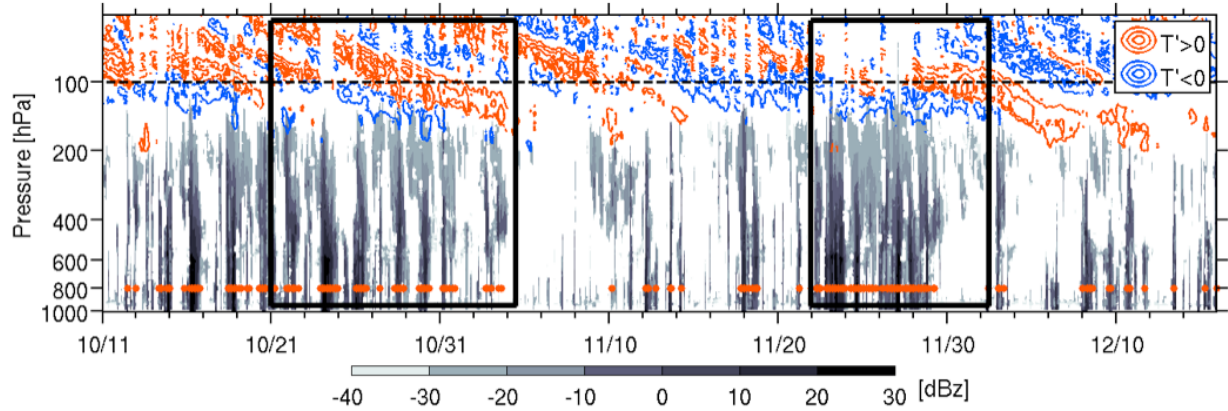
FIGURE 3.6. Time series of radar reflectivity (gray scale) from PNNL data averaged every two hours. Red dots denote deep convective cloud: times when ground-based radar or lidar detected cloud more than 50% of the time during the two-hour period, with a vertical extent of over 40% of the 150-1000 hPa column. Overlaid warm (red) and cool (blue) TTL temperature anomalies are contoured every 2 K. The 100 hPa pressure level (black dashed) is plotted for reference. Periods during RMM index phases two and three are boxed in black, corresponding to the active phase of the MJO over the Indian Ocean.

During the La Niña phase of the El Niño-Southern Oscillation, anomalously cool sea surface temperatures are seen with a cold tongue extending into the western Pacific Ocean from persistent equatorial surface easterly wind. Without the warm sea surface temperatures, Manus Island in the western Pacific would observe suppressed convection.

It is hard to get a sense of the horizontal scale of disturbances in the tropical tropopause layer when only looking at time series from two sites. Figure 3.7 shows temperature anomalies in various dimensions using ERA-Interim model data near the equator. The top panel is a time-longitude plot for the 95 hPa level, near the cold point tropopause. An overall seasonal cooling trend can be seen over the Maritime Continent. Prominent temperature anomalies are observed with the two MJOs, with strong cool anomalies present during the convectively active phases over the Indian Ocean and Maritime Continent as seen in Figure 3.6. The tilt of the features convey eastward propagation and a speed that would indicate a wave disturbance at Gan might travel a week before observations are seen at Manus.
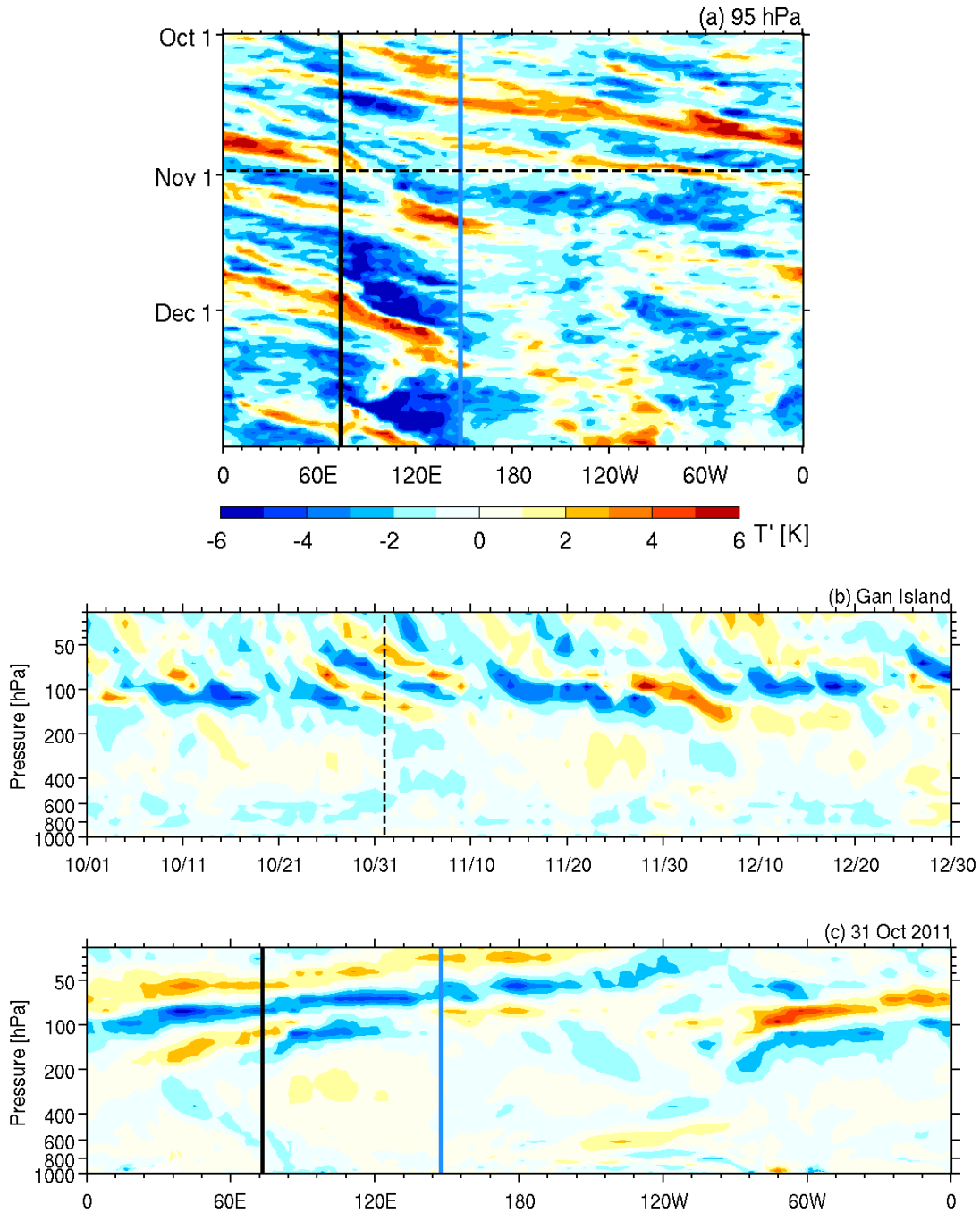
FIGURE 3.7. Temperature anomalies from ERAi model data taken at 0.4°S. (a) Time-longitude cross section at a vertical pressure of 95 hPa, near the cold point tropopause. (b) Pressure-longitude cross section on 31 October 2011, during the active phase of the MJO over Gan Island. (c) Pressure-time cross section at a longitude of 73°E, near Gan Island. Solid lines mark the longitude of Gan Island (black) and Manus Island (blue), and the dashed line marks 31 October 2011.

The center panel is a pressure-time plot for Gan Island and is similar to the temperature contours shown in Figure 3.6, but over an extended vertical layer. The warm anomalies near 300 hPa during the active phases of the MJOs in October and November, as well as the structure of the temperature anomalies extending into the lower stratosphere, resemble those first reported by Kiladis et al. (2001) using sounding data from Singapore and the western Pacific Ocean. The strongest wave activity is found above 150 hPa, where the high vertical stratification in the TTL allows atmospheric waves to freely propagate. The lower panel is a pressure-longitude plot for 31 October 2011, during the active phase of the MJO in the Indian Ocean. From this perspective, we see an eastward and upward tilt with height, consistent with downward phase propagation and upward energy dispersion. The prominent feature is a planetary-scale wave above 200 hPa. This global scale pattern in the temperature anomaly field closely resembles the findings of Virts et al. (2010) correlating a TTL cirrus index and filtered ERA temperatures. Convectively-coupled waves and the multiscale variability in the tropical tropopause layer will be analyzed in the next chapter. Their influence on cirrus cloud formation and radiative heating rates are discussed in Chapter 5.

The MJO and convectively coupled waves

4.1. Modulation of the cold point and lapse rate tropopauses

During DYNAMO, the tropical tropopause layer shows multiscale variability, including modulation by the Madden-Julian oscillation. The enhanced convection can impact the cold point and lapse rate tropopauses, as shown in Figure 4.1. Daily-averaged temperature profiles in the TTL are shown for Gan Island. The time-varying change in pressure level of both the cold point tropopause (CPT) and lapse rate tropopause (LRT) are indicated. During this period the mean CPT height is near 16.5 km, while the mean LRT height is found slightly lower. This is expected based on how each is calculated, as described in Section 2.2.2. Manus Island results (not shown) are similar, though the average heights are found higher in the atmosphere, which can be explained by differences in regional climatology (Fueglistaler et al. 2009).
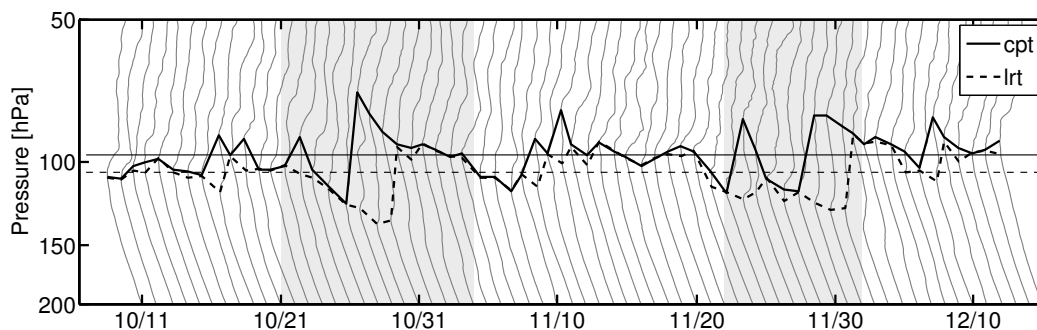
FIGURE 4.1. Time series of daily-averaged TTL vertical temperature profiles spaced by 10 K, from 2011 DYNAMO atmospheric sounding data over Gan Island. The trend in cold point tropopause (solid) and lapse rate tropopause (dashed) pressure levels are shown, as well as their October to December averages. Periods during RMM index phases two and three are shaded gray, corresponding to the active phase of the MJO over the Indian Ocean.

For both the CPT and LRT, the seasonal trend is seen as pressure decreasing (heights rising) from October to December. This seasonal change is related to the enhanced tropical upwelling by the Brewer-Dobson circulation in boreal winter (e.g. Yulaeva et al. 1994). On

an intraseasonal timescale, the two MJO active periods are highlighted and show common features. Observations suggest that modulation of tropopause height by the MJO is seen as a gradual increase in pressure (lower height) before a sudden jump up to lower pressure levels. There is a difference in timing between the CPT and LRT response, with the LRT pressure maximum lagging by approximately two days. Two peaks are observed in the CPT time series around the time of the November MJO that may be associated with wave activity, namely the two prominent Kelvin waves seen in the troposphere at this time (Johnson and Ciesielski 2013). Although daily averaging has smoothed out some of the higher frequency variability, smaller-scale fluctuations can also be seen throughout the period.

Tropopause temperature and height are related, with higher heights generally corresponding to colder temperatures. CPT and LRT temperatures are plotted in Figure 4.2. Manus Island is now included for comparison. Both locations show a seasonal temperature trend with temperatures dropping from October to December, in parallel with the intensified upwelling and rising heights discussed previously that would lead to adiabatic cooling. Throughout the DYNAMO time period, temperatures are typically colder and the overall seasonal trend is stronger at Manus than at Gan, due to the island's proximity to the west Pacific warm pool.

On an intraseasonal timescale, tropopause temperature responds with a warming followed by a cooling around the time of the MJO active phase for both locations. The pattern is not as clear as was seen with heights however, as there are considerable fluctuations in temperature throughout the period that are likely related to the presence of atmospheric waves. The initial rise in temperature, seen in late October at Gan and early November at Manus, amounts to a change of nearly 5 K and coincides with the midpoint of the MJO active phase determined by the RMM Index. The phasing of the peak in CPT in relation to the MJO is not consistent between sites for the November MJO, with the maximum temperature at Gan occurring at the end of the active phase, and the maximum temperature at Manus occurring just before the active phase. This might allude to a difference in wave activity associated with the two MJOs.
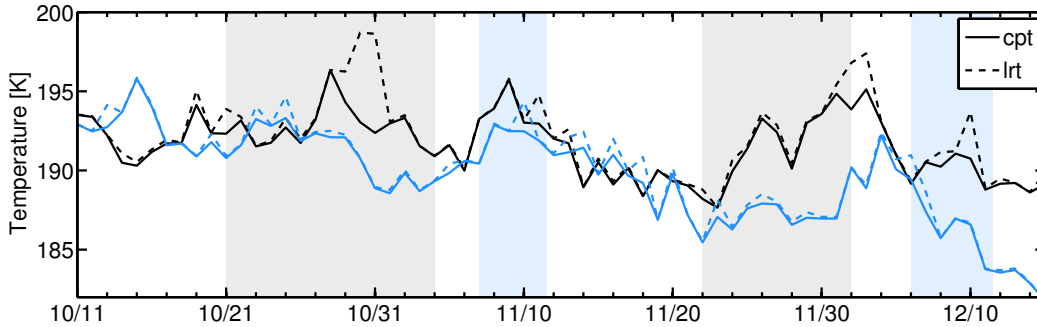
FIGURE 4.2. Time series of daily-averaged cold point tropopause (solid) and lapse rate tropopause (dashed) temperatures, from 2011 DYNAMO atmospheric sounding data over Gan Island (black) and Manus Island (blue). Periods during RMM index phases two and three are shaded gray, corresponding to the active phase of the MJO over the Indian Ocean. Periods during RMM index phases five and six are shaded light blue, corresponding to the active phase of the MJO over parts of the Maritime Continent and western Pacific Ocean.

There are several possibilities for the shifts seen in the thermal tropopause during DYNAMO. With the active phase of the MJO, increased convective latent heating in the middle and upper troposphere can induce a cooling at upper levels, particularly for deep convective clouds that penetrate high into the TTL (e.g. Paulik and Birner 2012). This local cool anomaly is an indirect response to convection and if cold enough could become the minimum temperature in the vertical profile, i.e. cold point tropopause. Another cause of variability is the passage of atmospheric waves that produce warm and cold anomaly layers in the region. In this scenario, the convection associated with the MJO is the energy source that excites a spectrum of equatorial waves that propagate in the TTL and lead to temperature changes. The intraseasonal fluctuations we see at Gan and Manus are likely a combination of the two. The MJOs during the field campaign had deep convective centers with overshooting cloud tops, and were a trigger for vertically-propagating waves, as seen in Figure 3.6.

The cold point and lapse rate tropopauses generally vary in unison. The greatest separation is seen during the two MJO active phases, and more so for Gan. Although they are both thermal tropopause measures, they are calculated differently and should be applied differently. The CPT is a direct measure of the actual temperature and is sensitive to anomalies from waves passing through. Since the CPT is located higher in the atmosphere, it

may pick up on signals in the lower stratosphere that the LRT is spatially removed from. High stratification in the stratosphere allows waves to vertically propagate more easily. The timing in lapse rate tropopause variability is consistent with a study by Tian et al. (2012) who used the LRT to examine global temperature patterns and vertical structure related to the MJO. Near the equator lower tropopause heights were found located to the west of regions of increased precipitation.

This timing corresponds to the minimum in LRT height lagging the minimum in CPT height seen in Figure 4.1. The delay in the response of the LRT is related to the downward phase propagation of the atmospheric waves. The impact of descending waves would first appear at higher levels. The LRT, which is located lower in the atmosphere than the CPT, would see the impacts later. Additionally, the LRT is based on temperature gradient which is influenced by moisture in the atmosphere. The LRT is closer to tropical convection, and may be related to the variability of the depth of convection during the MJO. In the presence of cloud and entrainment, there is often a sharp boundary in lapse rate between the upper troposphere and lower stratosphere. This creates a steep gradient in static stability, with implications for troposphere-stratosphere exchange and the vertical propagation of waves (Grise et al. 2010).

The variability seen in CPT and LRT temperature is due in part to the physical shift of the measured tropopause height with time. For instance, the sudden jumps in CPT seen in Figure 4.1 around 29 October and 1 December correspond to height changes of 2-3 km. Figure 4.3 shows the temperature trends for a constant pressure level of 130 hPa at both Gan and Manus from 3-hourly sounding data. Manus shows less variability overall, with temperature wavering no more than a few degrees from one timestep to the next. Gan results show greater variability with a significant jump on 4 December (also seen in Figure 3.6), though fluctuations are still generally under 5 K. During DYNAMO, the lowering of tropopause heights coincide with a slight warming. However, adiabatic warming would be greater based on the height difference, indicating that the change is not a purely adiabatic

one. A strong cold anomaly, such as the observed wave structure, must also be contributing to the local temperature.
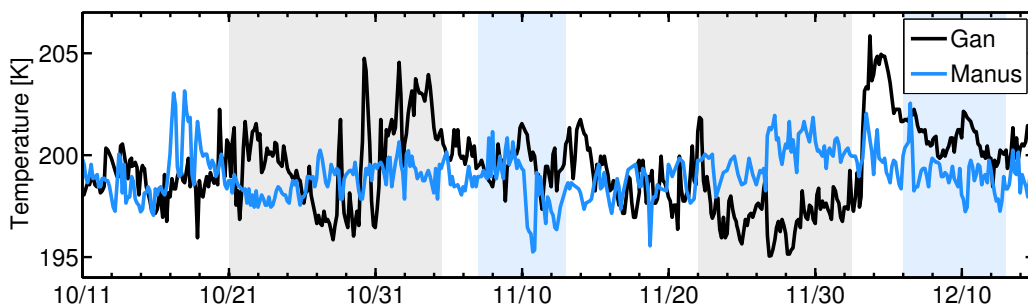
FIGURE 4.3. Time series of 3-hourly 130 hPa temperature from 2011 DYNAMO atmospheric sounding data over Gan Island (black) and Manus Island (blue). Periods during RMM index phases two and three are shaded gray, corresponding to the active phase of the MJO over the Indian Ocean. Periods during RMM index phases five and six are shaded light blue, corresponding to the active phase of the MJO over parts of the Maritime Continent and western Pacific Ocean.

Rapid changes in tropopause conditions are a result of wave activity in the TTL excited by MJO convection. The distinct Kelvin wave structure in Figure 3.6 shows a cold phase in the upper troposphere during the two MJO active phases and alternating warm and cold anomalies above. The top of convection ($\sim$130-200 hPa) and local diabatic cooling are found below the CPT, so that lower tropopause heights are a direct response to the cold phase of the upward propagating Kelvin wave. Just as the new cold point is established at that level, the Kelvin wave warm phase replaces the cold and the CPT follows the source of cooling, jumping back to upper levels where another cold phase may be found.

These results are similar to those of previous studies, such as Zeng et al. (2012). They note that temperature and specific humidity anomalies were significant prior to peak MJO convection and had an eastward tilt with height from the upper troposphere to the lower stratosphere. Since MJO enhanced deep convection acts to cool the tropopause, negative anomalies of CPT height and temperature were found to propagate eastward preceding MJO convection due to the tilted structure. The variation in CPT temperature anomalies were reported as $\sim$1.2 K near the equator with the variation in CPT height generally less than

∼200 m. These values are smaller than found in this study, and are likely an underestimate as four years of data were used to create a composited MJO cycle, whereas here we consider individual MJO events.

4.2. Multiscale variability in the TTL

From the distinct temperature structure, it is clear in Figure 3.6 that atmospheric waves are present during DYNAMO and have a strong influence on tropical tropopause layer characteristics. In this section we analyze the multiscale variability in the temperature and wind fields, and link them to several equatorial wave modes. Atmospheric waves are often a dynamical response to diabatic heating from tropical convection, though they have also been shown to arise from orographic effects as well as momentum forcing. As the Madden-Julian oscillation propagates from the equatorial Indian Ocean to the western Pacific, convection provides an energy source for waves to develop. Waves modes vary in both structure and dispersion characteristics, ranging from large-scale disturbances that propagate around the globe to smaller features that dissipate in a few hours. The Matsuno (1966) solutions of shallow water equations on an equatorial beta plane include Kelvin, equatorial Rossby, mixed Rossby-gravity, and intertio-gravity waves which fall along theoretical dispersion curves (Kiladis et al. 2009).

Several of these wave types are evident in DYNAMO observations. Figure 4.4 shows unfiltered anomalies of TTL temperature (T′), zonal wind (u′) and meridional wind (v′) at Gan Island. The 100 hPa level shown is near the cold point tropopause and captures some variability in both the upper troposphere and lower stratosphere. Similar features are seen at other levels, and at Manus Island as well (not shown). In comparing the temperature and wind fields, zonal wind appears to have the greatest variability. Large long-period fluctuations and smaller scale fluctuations show a range in periodicity and amplitude. The peaks in u′ near 1 November and 4 December suggest a roughly 30-day signal related to the Madden-Julian oscillation. In contrast, the peaks in u′ and T′ near 1 November and 10 November suggest a roughly 10-day signal associated with equatorial Kelvin waves. Higher

frequency fluctuations in both temperature and horizontal wind fields are seen throughout the three-month period, and suggest the presence of gravity waves that may be excited by convection.
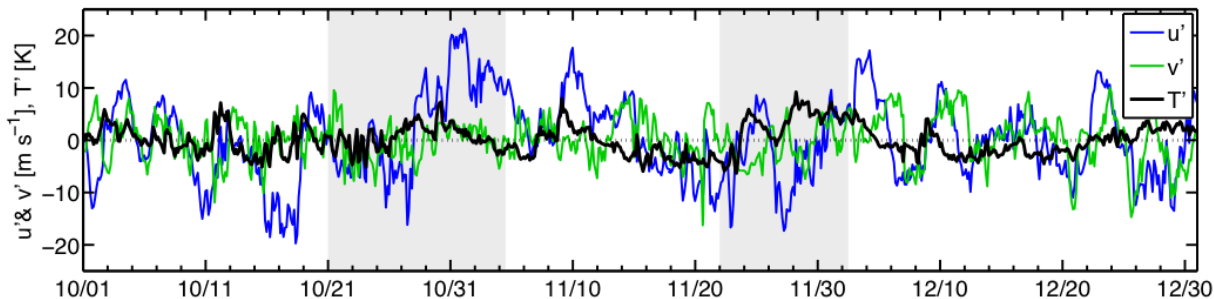
FIGURE 4.4. Time series of 3-hourly temperature (black), zonal wind (blue), and meridional wind (green) anomalies at 100 hPa, from 2011 DYNAMO atmospheric sounding data over Gan Island. Periods during RMM index phases two and three are shaded gray, corresponding to the active phase of the MJO over the Indian Ocean.

Spectral analysis is used to identify periodicity in the data, as described in Section 2.2.3. In the real atmosphere disturbances are not perfectly periodic, but this method can be useful in differentiating wave modes from background noise. Figure 4.5 shows the power spectra for the 100 hPa observations at both Gan and Manus. With temperature, zonal wind, and meridional wind anomalies plotted together, it is clear that the most prominent peaks are seen in the zonal wind field. The panels on the right show the zonal wind field replotted as a fraction of variance along with its estimated background red-noise spectra. The 99% significance level is based on the F-statistic, which tests the ratio of variances. At Gan Island, statistically significant peaks in the zonal wind are seen at periods of roughly 30 days, 12 days, and 5 days. These particular periods correspond with those expected for the MJO, Kelvin waves, and gravity waves, respectively.

Since DYNAMO atmospheric sounding data is limited to a three month period, a concern might be that unphysical peaks have been introduced due to the use of a finite dataset. To verify the robustness of results the analysis was repeated using daily-averaged ERA-Interim data over the 7-month period from August 2011 to February 2012. For Gan, statistically
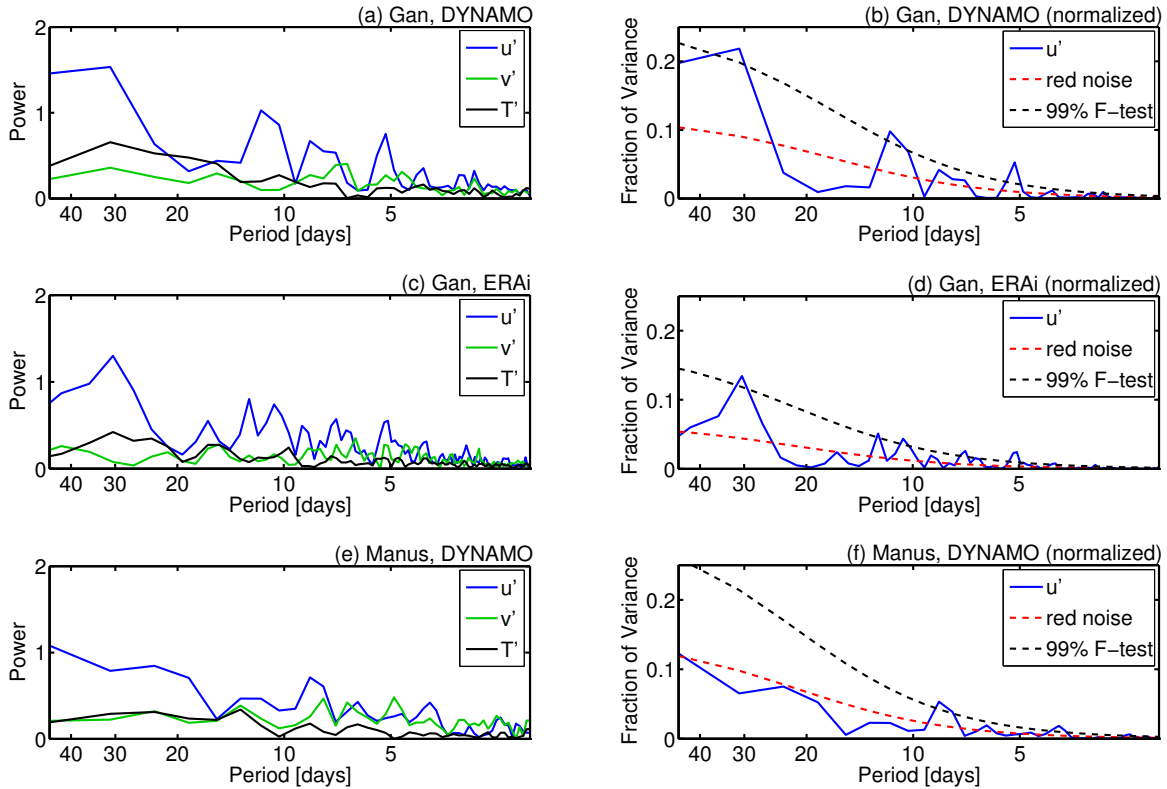
FIGURE 4.5. [Left] Power spectra of daily-averaged temperature (black), zonal wind (blue), and meridional wind (green) anomalies. [Right] Zonal wind spectra that have been normalized to show fraction of variance. The corresponding red-noise spectra (red dashed) and 99% significance levels (black dashed) are plotted for reference. (a,b) 100 hPa DYNAMO atmospheric sounding data at Gan Island over the 1 October to 31 December 2011 time period. (c,d) 95 hPa ERAi data at Gan Island over the 1 August 2011 to 29 February 2012 time period. (e,f) 100 hPa DYNAMO atmospheric sounding data at Manus Island over the 1 October to 31 December 2011 time period.

significant peaks in zonal wind anomalies are again seen for periods near 30 days, 12 days, and 5 days. The fraction of variance is smaller for the ERA-Interim data and additional peaks are seen at periods of 8 and 15 days, but overall it is a good match. The slight difference could be a result of the longer time period, which may include waves that peak outside of the October-December time frame as well as periods with minimal wave activity. Although seven months is not an extensive time period and windowing could still pose an issue, that the results are in close agreement gives us more confidence in the analysis. There is also physical reason to believe the peaks are meaningful, namely the intraseasonal timescale of the MJO and atmospheric waves.

Spectral analysis for Manus Island data shows the zonal wind variance is smaller than at Gan, suggesting reduced wave activity in the western Pacific Ocean. A statistically significant peak is seen for a periodicity near 8 days, which falls within the range for equatorial Kelvin waves. However, there is no clear signal related to the Madden-Julian oscillation. One reason for this could be that La Niña conditions with anomalously cool water in the Pacific Ocean, prevented MJO convection from making it to the site. Typically the MJO would continue to intensify into the western Pacific. However, in this situation the sea surface temperature may make environmental conditions unfavorable, causing the MJO to decouple from convection, suppressing the energy source for atmospheric waves. Gottshalck et al. (2013) note that the October and November MJOs both weakened as they propagated eastward, with MJO convection never reaching Manus Island in the western Pacific.

Wave signals in observations can overlap and are often incoherent. In these instances, filtering can be used to isolate the variability associated with the different wave modes. The prominent spectral peaks in the frequency spectra motivate the filtering of observations for the MJO, Kelvin wave, and gravity wave bands, as described in Section 2.2.4. Figure 4.6 shows the TTL vertical structure seen in filtered temperature and zonal wind anomalies at Gan Island during DYANMO. To isolate the MJO signal, data was bandpass filtered for periods between 20-80 days (Figure 4.6a). A 7-20 day bandpass was used to capture signals related to Kelvin waves (Figure 4.6b), while a highpass filter with a 7 day cutoff was used to separate out higher frequency waves (Figure 4.6c).
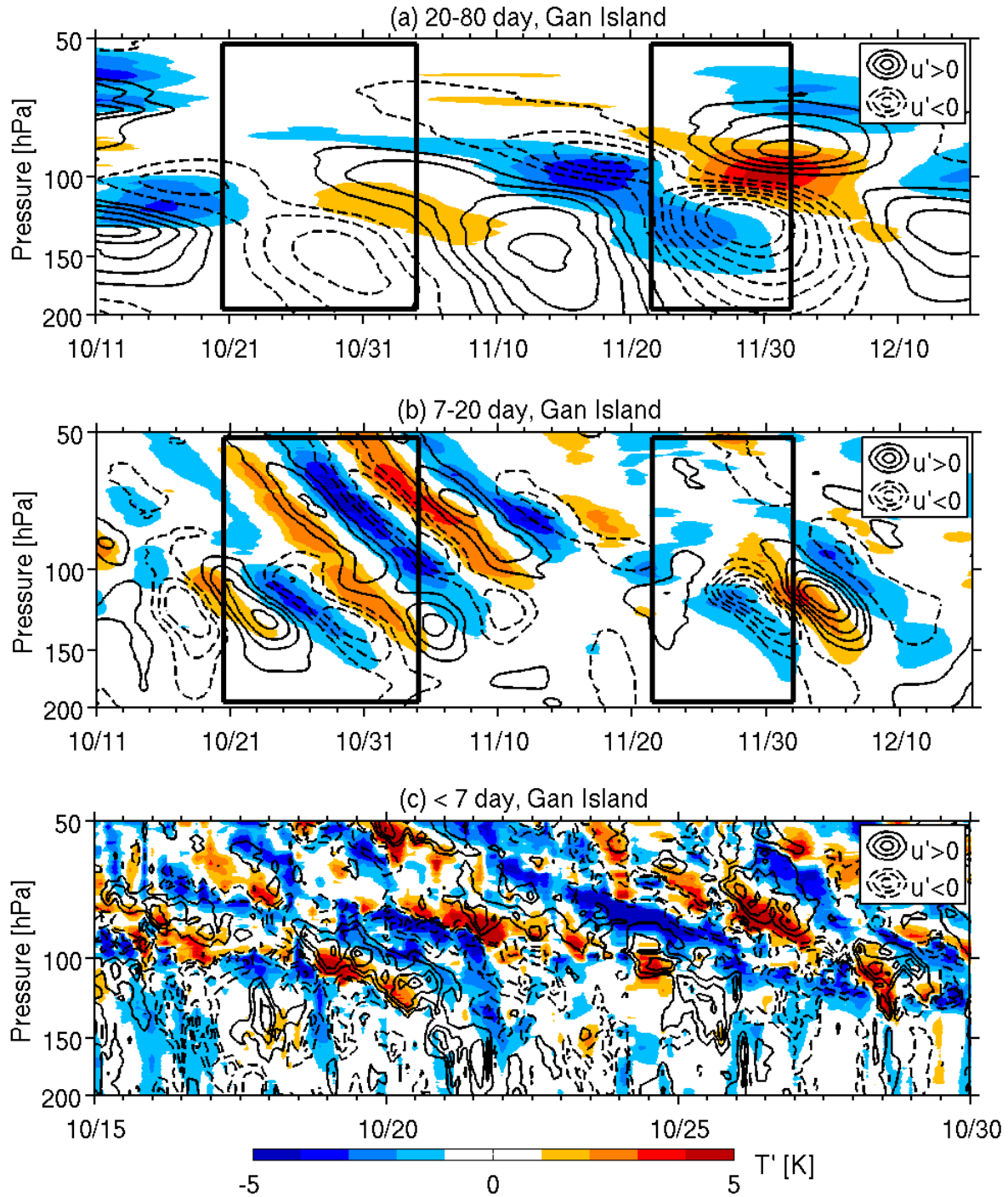
FIGURE 4.6. Time series of TTL temperature (color scale) and zonal wind anomalies (black contours), relative to the October to December mean vertical profiles (see Fig. 3.4). Zonal wind anomalies are contoured every 3 m/s with positive values indicating a stronger westerly component. DYNAMO atmospheric sounding data over Gan Island are shown with a (a) 20-80 day bandpass filter, (b) 7-20 day bandpass filter, and (c) 7 day highpass filter zoomed in on a 15 day period. Periods during RMM index phases two and three are boxed in black, corresponding to the active phase of the MJO over the Indian Ocean.

A 20-80 bandpass filter is used to isolate large-scale intraseasonal disturbances, such as the Madden-Julian oscillation. The MJO is a planetary scale phenomenon with a zonal wavenumber of 1-3 and is characterized by enhanced tropical convection in the troposphere during its active phase as seen in Figure 3.6. The approximately 30 day interval between the late October and late November MJO events seen at Gan Island during DYNAMO, puts this particular oscillation on the higher frequency compared to typical MJO frequencies observed in past studies. Signals are seen in both the temperature and zonal wind fields, with alternating positive and negative anomalies that slope downward with time. Eastward propagation is at a speed of $\sim$4 m s^{-1} over the Indian Ocean. Anomalous circulation associated with the MJO is seen as tropopause-level westerlies prior to (located to the east of) the active phase, with easterlies during and following (to the west of) peak convection. This corresponds to the expected upper-level divergence based on the MJO structure and lifecycle summarized in Figure 1.3. In the upper troposphere stronger MJO activity is seen in November compared to October, with easterly wind anomalies greater than 20 m s^{-1} and a cooling of $\sim$5 K. The signals in the temperature and winds field are not concurrent, with the cold anomaly maximum leading the easterly anomaly maximum by roughly 5 days. MJO signals taper off above 90 hPa, as the MJO is not a vertically propagating wave.

Strong convective diabatic heating is known to be able to excite a spectrum of waves, including convectively-coupled Kelvin waves that interact with the MJO (Kiladis et al. 2009). To isolate variability in the TTL related to equatorial Kelvin waves during DYNAMO, the data was bandpass filtered for periods of 7-20 days. The observed warm and cool anomaly pattern is the dynamic response to the vertical propagation of wave energy produced by MJO convection in the troposphere (Kiladis et al. 2001). High stratification supports vertical propagation in the TTL. Observations show three wave features in this frequency band. Similar Kelvin waves are seen in mid October and early December with a timescale of $\sim$13 days, and extend from 100-150 hPa with a strong cold anomaly during the active phases of the MJO. Additionally, a prominent Kelvin wave signal is seen in late October to early November with a timescale of $\sim$24 days and extending from 55-110 hPa. There is a striking

difference between Kelvin wave activity when comparing the October and November MJOs at Gan, as the active phase in late November does not show a Kelvin wave signal in the lower stratosphere. Interestingly, the November MJO is related to two prominent Kelvin waves observed in the troposphere, but these signals do not appear to translate to upper levels.

It is not clear why stratospheric conditions during the active phase of the October MJO were favorable for Kelvin wave activity while the active phase in November was not. There are several possibilities for this contrast. Differences in background horizontal flow could be one possibility, as mean flow is a critical factor in vertical wave propagation. As wave velocity approaches a background mean flow that is equal in magnitude, it is no longer able to sustain propagation and will eventually "break". For Kelvin waves, this occurs in a westerly mean flow. Figure 3.2 does not show a notable change in stratospheric zonal wind during DYNAMO. There is a persistent westerly phase of the QBO in both October and November. Similarly, interactions with other modes of variability in November could complicate things. If waves with significant westward propagation were also present, they could act to mask or impede Kelvin wave activity. Another idea is that the data set is limited by the location of Gan Island. A Kelvin wave may be present, but the signal is not pronounced at this particular site.

Perhaps the most compelling argument is that the lower stratospheric wave in October is a free planetary-scale Kelvin wave uncoupled to any forcing. It may have been excited outside of MJO convection and was able to vertically propagate into the lower stratosphere. In this case, it is coincidental that during its eastward propagation around the globe, the timing at Gan Island aligned with MJO convection over the Indian Ocean. It is curious though, that the tilted structure and the propagation speed are similar between the upper tropospheric waves and the lower stratospheric wave in October. Free (dry) wave modes typically travel at faster phase speeds than their convectively-coupled counterparts and are primarily observed in the stratosphere. The average phase speed (relative to the ground) in a dry atmosphere is 25 m s^{-1} (Andrews et al. 1987). In a region of convective heating the effective stratification is reduced which acts to slow wave propagation. Further research

would be needed to determine the true origin of the wave, and if it has any connection to the MJO. If we assume the stratospheric Kelvin wave is a free mode and disregard wave activity above ∼90 hPa, the remaining upper tropospheric disturbances can be considered as the Kelvin wave response to the Madden-Julian oscillation. Although the timing varies, with waves present during peak MJO convection in October and lagging peak convection in November, the characteristics of the two Kelvin waves are similar in terms of vertical extent and phase velocity.

In this analysis we have characterized atmospheric waves based on temperature and zonal wind anomalies. One thing to note is that the same vertical structure is not seen in the meridional wind field (not shown) in this frequency range, suggesting that Kelvin waves are the dominant wave mode. These waves are equatorially-trapped, meaning they are constrained to low latitudes where the equator acts as a boundary. They preferentially propagate eastward due to the rotation of the Earth and generally require a background easterly wind regime, though they may exist in weak westerlies. For Kelvin and higher frequency gravity waves, gravity is the restoring force needed to sustain propagation. Andrews et al. (1987) describe typical zonal wind and temperature anomalies of $u' = 8$ m s^{-1} and $T' = 2\text{-}3$ K for Kelvin waves. The anomalies observed at Gan Island are coupled to MJO convection and have stronger amplitudes, with $u' = 15$ m s^{-1} and $T' = 4$ K. The structure of the TTL anomaly fields suggests an approximate covariation in temperature and zonal wind. The vertical and horizontal wavelengths are the same for temperature and zonal wind fields, but warm (cool) anomalies precede westerly (easterly) anomalies by ∼2 days. A quadrature phase relationship is expected for an idealized eastward propagating Kelvin wave in constant background flow ($\bar{u} = $ const.). From linear wave theory vertical advection is out of phase with temperature but in phase with zonal wind. It follows that temperature oscillations should lead the zonal wind oscillations by a quarter cycle (Holton and Hakim 2013).

Strong temperature and zonal wind anomalies above 150 hPa exhibit a downward slope with time, as predicted for a vertically propagating Kelvin wave. The tilt describes a downward phase velocity, perpendicular to upward energy dispersion. Group velocity and phase speed of the disturbance can be estimated using the dispersion relation for equatorial Kelvin waves (Andrews et al. 1987).

$$(4.1) \qquad\qquad \omega_d \equiv \omega - k\bar{u} = -Nk/m,$$

where ω_d is the intrinsic frequency, ω is the frequency relative to the ground, $\bar{u}$ is the mean zonal wind, and N (2.2 x 10^{-2} s^{-1} in the stratosphere) is the Brunt-Väisälä (buoyancy) frequency. k and m are the zonal and vertical wavenumbers, respectively.

Based on this dispersion relation, the zonal phase speed of the convectively-coupled wave in late October was estimated as 13.7 m s^{-1} (10.6 °lon day^{-1}). The vertical wavelength λ_z = 3.9 km used in the calculation is based on the extent of the warm anomaly from 100-140 hPa on 21 October, which corresponds to half a wavelength. The 10 day period of the wave is based on the warm anomaly from 21-26 October at 120 hPa, which corresponds to half of the period. Rapid dissipation of the wave above ~100 hPa coincides with the strong vertical wind shear in the transition from easterlies below to westerlies above seen in Figure 3.2. The convectively coupled Kelvin wave observed in early December in association with the MJO active phase has a similar vertical structure and phase speed.

For comparison, the calculations are repeated for the large-scale lower stratospheric wave observed in late October and early November. The Kelvin wave zonal phase speed was estimated as 14.7 m s^{-1} (11.4 °lon day^{-1}), based on a vertical wavelength λ_z = 4.2 km from the half wavelength determined by the warm anomaly between 85-125 hPa on 31 October. The 12 day period is based on the 31 October and 6 November period at 125 hPa. This wave is only marginally faster than the upper tropospheric Kelvin waves, but is of much larger scale. ERA-Interim longitudinal data reveals it is a planetary-scale wave with zonal wavenumber 1, compared to wavenumber 3-4 for the convectively-coupled upper tropospheric

waves (not shown). In October, the timing of the two Kelvin wave disturbances overlap by several days at the end of the month. The positive temperature anomalies seem to vertically align, and may suggest wave interference near the cold point tropopause.

The Kelvin wave characteristics shown for DYNAMO are comparable to those of previous studies. Holton et al. (2001) observed a lower stratospheric zonal wavenumber 2 wave with a 9.5 day period and vertical wavelength of 4.5 km. Much like the Kelvin waves observed at Gan, the phase speed was estimated to be around 14 m s^{-1}. Andrews et al. (1987) provide a summary of typical Kelvin wave characteristics, noting a period of 15 days, zonal wavenumber 1-2, and vertical wavelength of 6-10 km. The Kelvin waves observed during DYNAMO have a shorter vertical wavelength, which is often the case in regions of high stratification such as the lowermost stratosphere ($m \sim N$). Kelvin waves typically propagate more slowly over the Indian Ocean due to interaction with convection and speeds typically range from 12-15 m s^{-1} in this region. We find that the calculated wave phase speeds at Gan fall within this range. Over the west Pacific Ocean eastward phase speeds are closer to 15-20 m s^{-1} (Kiladis et al 2009).

Comparing the two convectively-coupled waves, the amplitudes of the zonal wind and temperature anomalies are greater for the early December disturbance. The zonal wind peaks around 15 m s^{-1}, compared to the peak amplitude of 9 m s^{-1} associated with the wave in late October. Since the magnitude of the Kelvin wave response is dependent on the strength of convection below, this result is consistent with the stronger MJO signal seen in the 20-80 day filtered observations as well as analysis of the tropospheric waves noted in previous studies. This suggests that although there are similarities between the MJO events, the two are dynamically different and generalizations about TTL variability associated with the Madden-Julian oscillation cannot be made based on this dataset.

Higher-frequency time scales were isolated using a highpass filter for frequencies corresponding to periods less than 7 days. Figure 4.5 shows a slight peak in the meridional wind power spectra which would suggest that at least a portion of the variability is not related to equatorial Kelvin waves. A spectrum of smaller-scale waves account for the remaining

variability. In general, both temperature and wind anomalies slope downward with time, though the vertical structure is not well-defined and suggest the presence of both eastward and westward propagating waves. The greatest temperature anomalies seem to fall within the 70-100 hPa layer in the lower stratosphere where there is stable stratification. Modulation by the Madden-Julian oscillation does not seem to be present, as there is no appreciable change in wave activity during the MJO active phase.

The higher frequency variability encompasses a broad spectrum of waves, including equatorial Rossby (westward), mixed Rossby-gravity waves (westward), and inertio-gravity waves excited by convection. Equatorial Rossby waves are typically one of the dominant modes of westward moving variability in the tropics, but activity was relatively weak throughout DYNAMO (Gottschalck 2013). Gravity waves are commonly excited by tropical convection, although other forcings include air flow over topography and local squall lines. Gravity waves and the influence on large-scale dynamics will be discussed further in Section 4.2.

Figure 4.7 shows temperature and zonal wind anomalies that have been frequency filtered to separate Madden-Julian oscillation, Kelvin wave, and higher-frequency wave modes for Manus Island. 20-80 day bandpass filtering shows only a weak signal in the MJO band in early December. This is consistent with Figure 4.5 in which no statistically significant spectral peak was found for an intraseasonal timescale. Filtering for frequencies corresponding to periods of 7-20 days reveals Kelvin wave activity in early November. Alternating warm and cool anomalies vertically extend from 50-110 hPa (4.4 km) with a period of almost two weeks. In general, the amplitude of the wave is smaller than was observed at Gan Island. There is no coherent signal seen with the 7 day highpass filtering due to a broad spectrum of higher-frequency wave modes.

In comparison to Figure 4.6, the differences seen in the 20-80 day and 7-20 day filtered observation are consistent with weakened atmospheric wave signals at Manus Island. MJO convection did not make it to the western Pacific Ocean, which is likely related to the La Niña conditions during DYNAMO. The convectively coupled Kelvin waves seen in the upper troposphere at Gan during the MJO active phases are not apparent at Manus. There is still
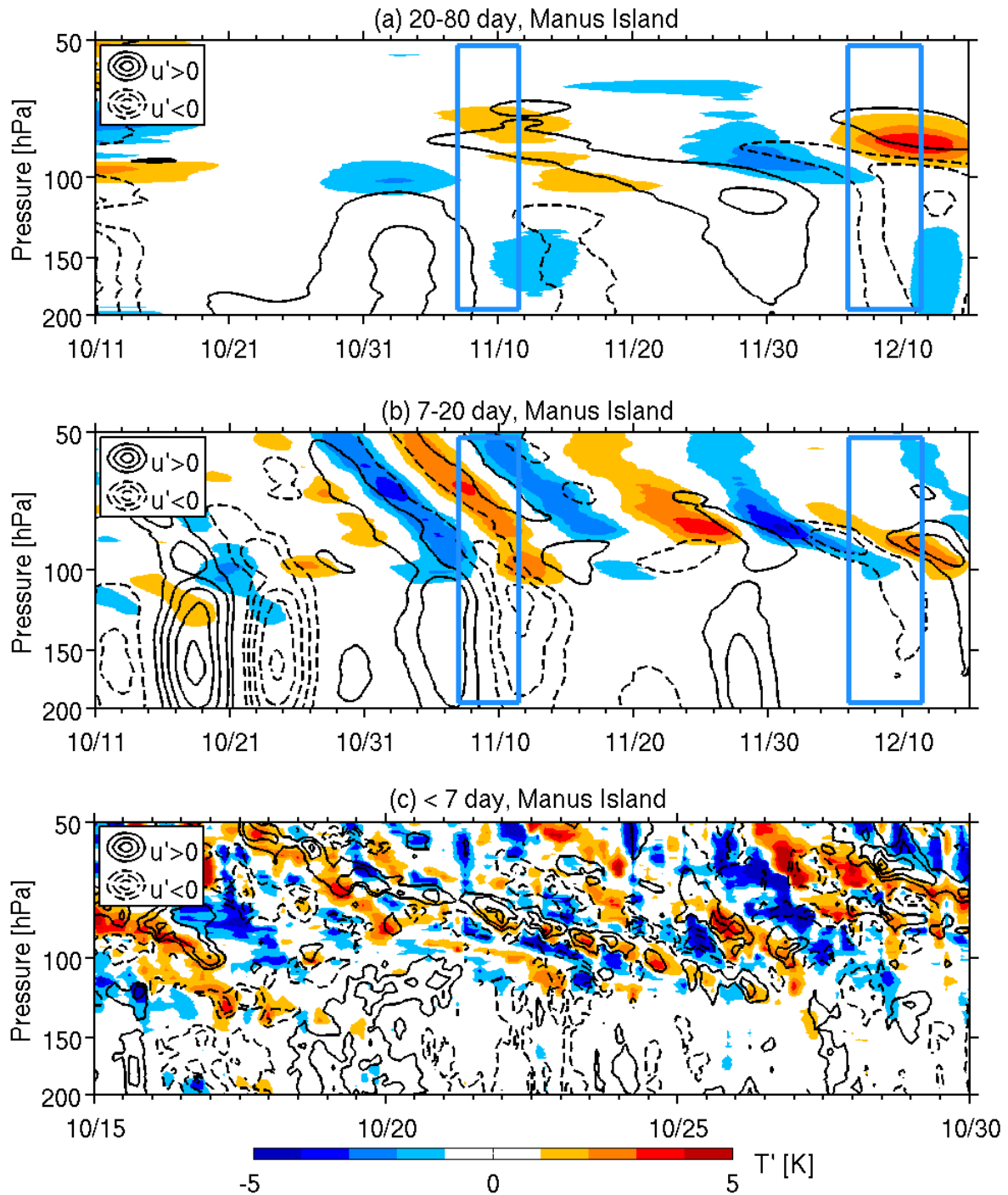
FIGURE 4.7. Time series of TTL temperature (color scale) and zonal wind anomalies (black contours), relative to the October to December mean vertical profiles (see Fig. 3.4). Zonal wind anomalies are contoured every 3 m/s with positive values indicating a stronger westerly component. DYNAMO atmospheric sounding data over Manus Island are shown with a (a) 20-80 day bandpass filter, (b) 7-20 day bandpass filter, and (c) 7 day highpass filter zoomed in on a 15 day period. Periods during RMM index phases five and six are boxed in blue, corresponding to the active phase of the MJO over parts of the Maritime Continent and western Pacific Ocean.

a signal in the planetary-scale stratospheric wave seen at Gan at the end of October, though it dissipates somewhat during the eastward propagation from the central Indian Ocean to the western Pacific. Estimating a constant group velocity of 14.7 m s^{-1} from the dispersion relation in Equation 4.1, and a background flow of 10 m s^{-1} based on the mean vertical profile in Figure 3.4 at 60 hPa, the disturbance at Gan should roughly take 3.9 days to reach Manus Island. This is a good approximation for the travel time observed. This further supports the idea that the lower stratospheric disturbance is a free wave mode that does not rely on continued organized convection. Gravity waves are present throughout the time period and likely have energy sources unrelated to MJO convection, as well.

4.3. Lower stratospheric wave analysis

Atmospheric waves can modulate the vertical transport of water vapor and other constituents between the troposphere and stratosphere by modulating the cold point tropopause, as discussed in Section 4.1. Furthermore, theoretical work by Booker and Bretherton (1967) established that in the presence of vertical wind shear, waves redistribute zonal momentum vertically in the atmosphere. In approaching the critical level, the point at which phase speed and horizontal mean flow are equal, vertically-propagating waves dissipate and deposit momentum. The wave-mean flow interaction goes both ways, where background wind conditions are important for wave propagation, and waves produce a forcing on the local mean flow. The net forcing depends on the spectrum of waves present. Waves that make it into the stratosphere drive the phase of the quasi-biennial oscillation (QBO). Upward propagating Kelvin waves are a source of westerly momentum. Alexander and Holton (1997) found that gravity waves provide nearly a quarter of the zonal forcing needed for the QBO.

From horizontal wind and temperature data, atmospheric wave amplitudes and the direction of horizontal propagation can be determined. Wave perturbations are used to calculate the contribution of waves to energy and momentum transport and the resulting force on the background atmosphere. Previous studies (e.g. Allen and Vincent 1995; Wang and Geller 2003) have looked at latitudinal and seasonal patterns, and found that lower latitudes and

boreal winter tend to have stronger lower stratospheric gravity wave energy. They used a polynomial fit to approximate the background mean vertical structure, so that gravity wave perturbations were calculated as the difference between the raw sounding observations and the fit.

In this study we consider lower stratospheric waves during DYNAMO, focusing on the 30-85 hPa layer due to data availability, to determine if there is a dynamical response to MJO convection. Wave energy per unit mass (energy density) is found as described in Section 2.2.5. The 30-85 hPa layer corresponds to roughly 6.2 km which means the large vertical wavelengths may not be well captured in each sounding profile. The seasonal mean background profile is removed through filtering of the data, in order to extract wave fluctuations in zonal wind, meridional wind, and temperature. With this analysis, temperature perturbations can be related to the potential energy, and wind perturbations can be related to the kinetic energy of the waves.

The relative contributions of temperature and wind deviations to lower stratospheric wave energy are plotted. Figure 4.8a shows the results for Gan Island with 7-20 day bandpass filtering to isolate frequencies associated with equatorial Kelvin waves. Zonal wind shows the strongest signal with an average peak energy density of $\sim$13 J kg^{-1} in late October to early November. Temperature amplitudes are in phase and lead to a peak energy density of $\sim$7 J kg^{-1} around the same time. This indicates that zonal kinetic energy density is nearly twice as large as potential energy density during the first MJO active period. Less prominent peaks are also seen in early December during the second MJO active period, which is likely a minor contribution from the convectively coupled Kelvin wave in the upper troposphere. The energy associated with the meridional wind is near-zero throughout the time period, as expected for a Kelvin wave response. Gill (1982, p. 261) provides a summary table for wave properties. For hydrostatic and non-rotating conditions, which lead to a similar dispersion relation as Kelvin waves, the ratio between potential and kinetic energy is close to one. The difference between observations and theory could be an outcome of the parameters chosen for our analysis, and the limited vertical extent of the dataset.
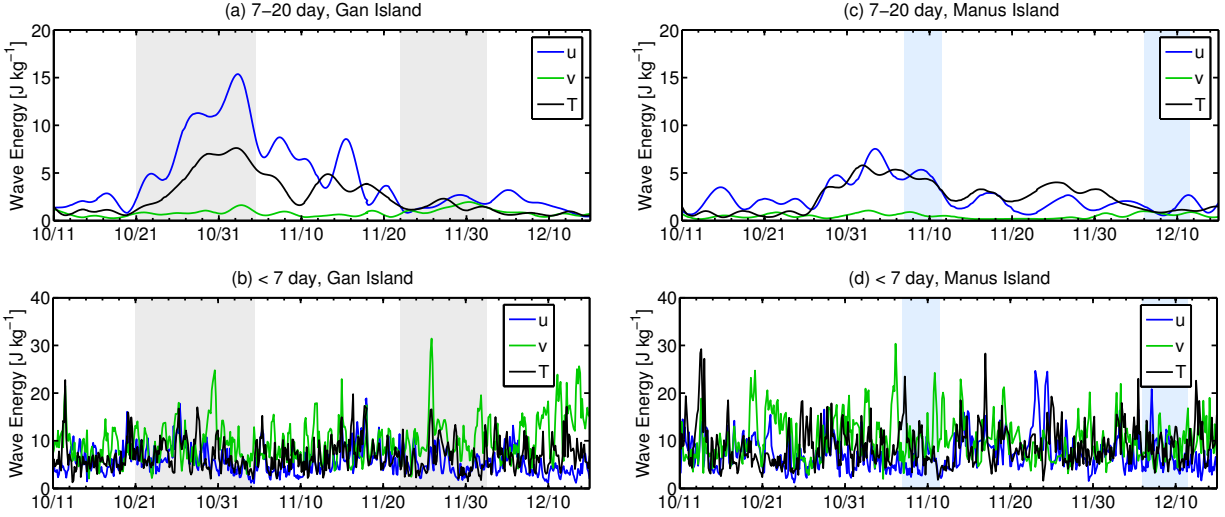
FIGURE 4.8. Time series of lower stratospheric wave energy, with contributions from temperature (black), zonal wind (blue), and meridional wind (green) from 2011 DYNAMO atmospheric sounding data. Wave energy calculations are based on variances, with averages taken over the 30-85 hPa vertical layer. (a) Gan Island data with 7-20 day bandpass filter. (b) Gan Island data with 7 day highpass filter. Periods during RMM index phases two and three are shaded gray, corresponding to the active phase of the MJO over the Indian Ocean. (c) Manus Island data with 7-20 day bandpass filter. (d) Manus Island data with 7 day highpass filter. Periods during RMM index phases five and six are shaded light blue, corresponding to the active phase of the MJO over parts of the Maritime Continent and western Pacific Ocean.

At Manus Island (see Figure 4.8c) zonal wind and temperature contributions to energy density are comparable, with peak energy densities of $\sim$5 J kg^{-1}, lagging approximately 3-4 days behind the peaks seen at Gan. The contribution from meridional wind is again negligible for the Kelvin wave response. Amplitudes appear dampened and the wave signal has showed signs of dissipation in the background westerly mean flow of the lower stratosphere. Total wave energy has decreased by nearly half, from roughly 20 J kg^{-1} to 11 J kg^{-1}. The ratio between potential and kinetic energy density is nearly one-to-one, which is different than was found for Gan Island where the zonal wind to temperature ratio increased during the MJO active phase. This suggests that the Kelvin wave slowed during propagation, dissipating and transferring momentum to the background mean flow.

Figures 4.8b and 4.8d show the lower stratospheric wave energy at Gan and Manus after a high pass filter with a cutoff period of 7 days has been applied in order to remove the contribution from longer period waves. On average the higher frequency disturbances, such as gravity waves, have greater wave energy density in all three fields than for the 7-20 day bandpass. Amplitudes show roughly equal contributions from temperature, zonal wind, and meridional wind. There is a spike in energy density at Gan on 25 November, which is likely a strong westerly wind burst from a large amplitude wave during that time. Overall, the meridional wind contribution to energy is slightly higher with an average amplitude near 10 J kg^{-1} at Gan. Zonal wind and temperature energy contributions are roughly 6 J kg^{-1} and 8 J kg^{-1}, respectively. Adding the contributions from zonal and meridional wind, we find that the kinetic wave energy is roughly double the potential energy. This is opposite that of the Kelvin wave response seen at Gan, suggesting different properties between the wave modes.

For comparison, Zhang et al. (2013) studied 11 year averaged latitudinal and altitudinal variations in lower stratospheric wave energy. They found the maxima of the potential energy density to be around 13.5 J m^{-3}. The kinetic energy density contribution from zonal wind was 6.7 J m^{-3}, and the contribution from meridional wind was comparable at 7.1 J m^{-3}. The total kinetic energy is similar in magnitude to the potential energy, as expected from theory.

At Manus the amplitudes show greater fluctuations and a higher average energy density than at Gan, which is attributed to regional convection. At both sites wave energy is substantial throughout the time period, with no clear response to the MJO. The high abundance of gravity waves in the lower stratosphere suggests there are several sources including topographical influences and the generation of gravity waves by deep convection with strong vertical motion (Fovell et al. 1992). The total wave energy density is the sum of kinetic and potential energy densities, and is greater for gravity waves than the lower stratospheric Kelvin wave seen during DYNAMO.

To explore the possible influence of the Madden-Julian oscillation on lower stratospheric wave energy, we compare the two MJOs during DYNAMO. Although peak wave energy aligns with peak convection during the first MJO active phase, we see dramatically reduced

peaks for the November MJO with the 7-20 day bandpass. This corresponds to what was shown in Figure 4.6, with a free planetary-scale Kelvin wave signal in late October to early November and a lack of signal during the second MJO active phase. Based on this dataset, the Madden-Julian oscillation has no appreciable impact on the lower stratospheric wave energy in either Kelvin wave or gravity wave frequencies, though the MJO may modulate wave energy in the upper troposphere. Ideally, a larger dataset would be used to produce MJO composites of gravity wave energies to determine if there is modulation by the MJO.

The variation in zonal and meridional momentum fluxes can be calculated by incorporating fluctuations of vertical velocity, as previous studies have done. Further analysis could also be used to extrapolate the intrinsic frequency of the waves based on the different energy density components, and look at the ratio of the intrinsic frequency to Coriolis parameter. This is beyond the scope of this study, but would be interesting future work.

CHAPTER 5

Cirrus clouds and the effect on radiative heating

5.1. Tropopause-level cirrus clouds

We would expect the structured temperature anomaly field seen in Section 4.2 to correspond to higher relative humidity during the cold regions, and therefore increase the likelihood of cirrus formation. However, ground-based instrumentation at Gan Island was not able to detect thin, high clouds during DYNAMO, see Figure 3.6. TTL relative humidity with respect to ice is calculated from saturation vapor pressure, as described in Section 2.2.6, and is shown in Figure 5.1. Cold anomalies based on the October-December mean are overlaid for comparison. At Gan Island, increased relative humidity is seen below the cold point tropopause during the active phase of the MJO, and coincides with the descending Kelvin wave cold phase triggered by MJO convection. In particular, there is a descending wave signal with an amplitude of 4-5 K around 100-150 hPa in late November which coincides with relative humidity of greater than 80%.

The correlation between high relative humidity and cold temperature anomaly is observed at several other times throughout the time period, including late October during the active phase of the MJO. The tilt with height suggests the moisture field follows the MJO convective system with eastward propagation. Although high relative humidity and supersaturation (RH > 100%) conditions are seen in the TTL, actual water vapor concentrations may be low with little variation. It is variation in temperature that drives changes in relative humidity and creates conditions that are favorable for cirrus cloud occurrence. Outside of the cold phase of the Kelvin waves, lower relative humidity is seen.

Observed zonal-mean values of relative humidity with respect to ice at 147 hPa is 85% in the tropics (Sandor et al. 2000). The coldest TTL temperatures are found in the western Pacific Ocean. Relative humidity at Manus is less variable throughout the time period than seen at Gan, with a consistently high percent relative humidity below 70 hPa from October to December. There is an apparent seasonal cycle with the relative humidity signal gradually
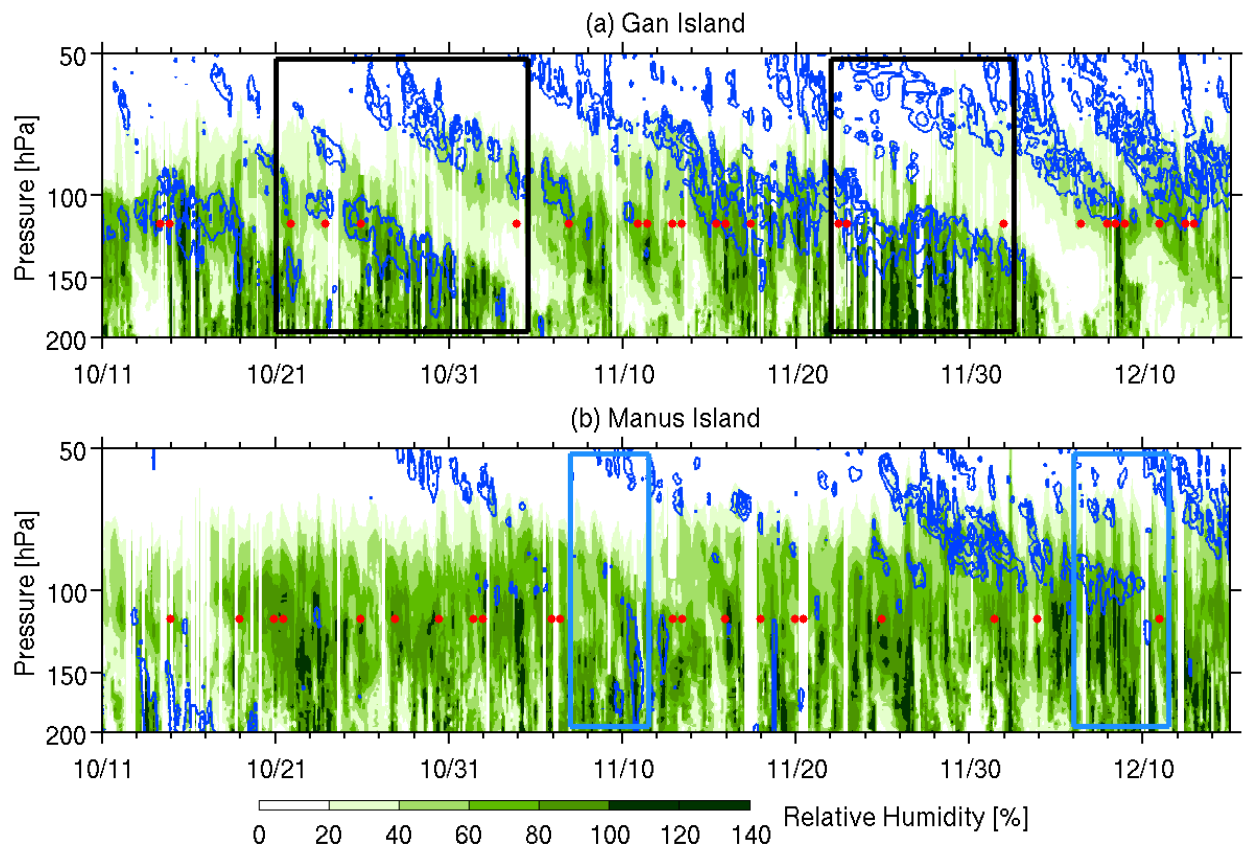
FIGURE 5.1. Time series of 3-hourly TTL relative humidity with respect to ice (green scale), calculated from temperature and dew point using 2011 DY-NAMO atmospheric sounding data. Cold temperature anomalies (blue contours), relative to the October to December mean vertical profile, are contoured every -2 K. Red dots represent times when it appears cirrus clouds are present, based on CALIPSO cloud layer fraction profiles (see Fig. 5.2). (a) Gan Island data. Periods during RMM index phases two and three are boxed in black, corresponding to the active phase of the MJO over the Indian Ocean. (b) Manus Island data. Periods during RMM index phases five and six are boxed in blue, corresponding to the active phase of the MJO over parts of the Maritime Continent and western Pacific Ocean.

extending higher into the TTL in boreal winter. Kelvin wave structure at Manus is not distinct as it was at Gan, suggesting little or no modulation by the MJO in this region during DYNAMO.

The formation of cirrus is limited to regions where the relative humidity is sufficiently high. This strong dependence of saturation vapor pressure on temperature is given by the Clausius-Clapeyron equation, which describes the rate of change of water vapor with respect to changes in temperature under typical atmospheric conditions (Bohren and Albrecht 1998).

$$(5.1) \qquad \frac{de_s}{dT} \approx \frac{L_v(T)e_s}{R_v T^2}$$

where e_s is the saturation vapor pressure, T is temperature, L_v is the latent heat of vaporization of water, and R_v is the gas constant for water vapor.

Higher cirrus cloud frequencies should coincide with the colder temperatures and higher relative humidity. This is consistent with a study by Sandor et al. (2000) that found a strong positive correlation between mean relative humidity with respect to ice and the percent occurrence of cirrus clouds. They found that on average, 100% relative humidity near the tropopause corresponded to a 50% occurrence of cirrus, and 140% relative humidity typically corresponded to 80% cirrus frequency.

Equatorial waves associated with the MJO likely create favorable conditions for cirrus cloud formation, particularly during the descending Kelvin wave cool phase ahead of MJO peak convection. In this study, we use CALIPSO satellite data to determine when cirrus clouds were present and relate them to temperature variability in the TTL. A disadvantage of CALIPSO data is that sampling is coarse both temporally and spatially, as described in Section 2.1.3. Figure 5.2 shows cloud layer fraction at Gan Island and Manus Island. In contrast to Figure 3.6 there are instances when clouds extend above 100 hPa.

At Gan, cloud top heights (outlined) show an increase in mid-October and mid-November in the week prior to the MJO active phase. There is an overall trend of increasing cloud top height with time, particularly at Manus. This is the seasonal cycle, with colder TTL temperatures seen in boreal winter. At Manus, cloud top height does show a clear relationship with the MJO active phase.
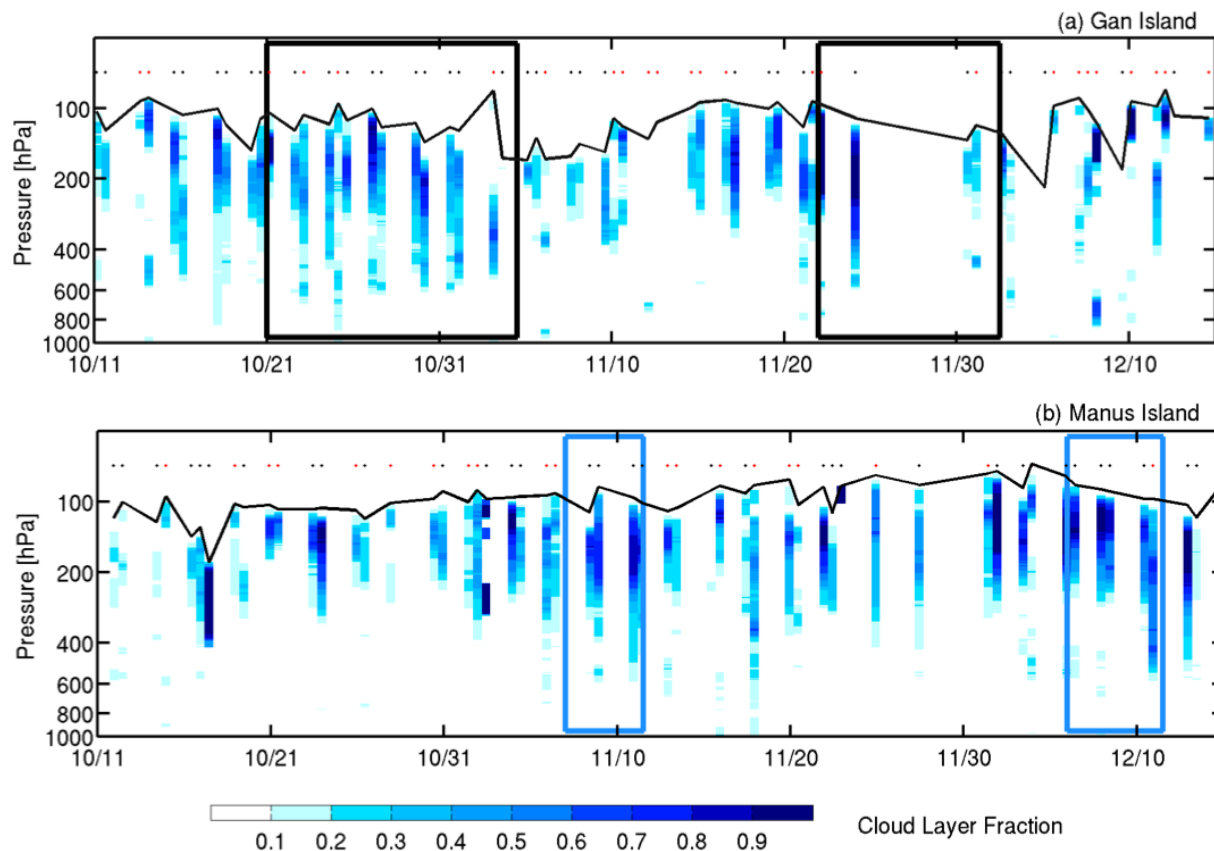
FIGURE 5.2. Time series of cloud layer fraction profiles, from 2011 CALIPSO satellite data averaged over a 10°-latitude x 10°-longitude box. Dots denote times when profiles are available, with red dots representing times when it appears cirrus clouds are present. The black line shows the trend in detected cloud top height. (a) 10°-latitude x 10°-longitude box centered around Gan Island. Periods during RMM index phases two and three are boxed in black, corresponding to the active phase of the MJO over the Indian Ocean. (b) 10°-latitude x 10°-longitude box centered around Manus Island. Periods during RMM index phases five and six are boxed in blue, corresponding to the active phase of the MJO over parts of the Maritime Continent and western Pacific Ocean. Note: column width is not to scale, as each overpass is no longer than a few minutes.

The timing of CALIPSO overpasses are indicated by dots at the top of each figure. At times when tropopause-level cirrus clouds were detected, the dots are marked red. Note that the absence of cirrus at certain times may be due to the infrequency of CALIPSO data and not an indication of cloud conditions. The timing of observed cirrus clouds are also marked in Figure 5.1 to show the relationship between atmospheric waves, relative humidity, and cirrus clouds seen on an intraseasonal timescale. At Gan Island, there appears to be an increase in

tropopause level cirrus ahead of the MJO active phase in accordance with the Kelvin wave cold phase and higher relative humidity. Manus Island does appear to have a trend in cirrus cloud occurrence. There is a greater frequency of cirrus year round in the western Pacific and at higher altitudes following the coldest temperatures (Sassen et al. 2008).

These results are consistent with a study by Boehm and Verlinde (2000) who found that cirrus clouds near the tropopause are related to temperature perturbations of the equatorial Kelvin wave. Past studies (e.g. Del Genio et al. 2012, Eguchi and Shiotani 2004, Virts and Wallace 2013) have also described the typical cloud structure in relation to MJO phase, with cirrus clouds leading peak convection. The cold anomalies associated with the MJO have the signature of equatorially trapped Kelvin waves. The descending upper level cool anomalies and cold point tropopause heights that precede the active phase of the MJO, allows water vapor to condense and clouds to form. Kelvin wave structure plays an important role in dehydrating air through this freeze-drying mechanism. As such, the Kelvin wave cold phase is typically followed by anomalously low water vapor concentrations.
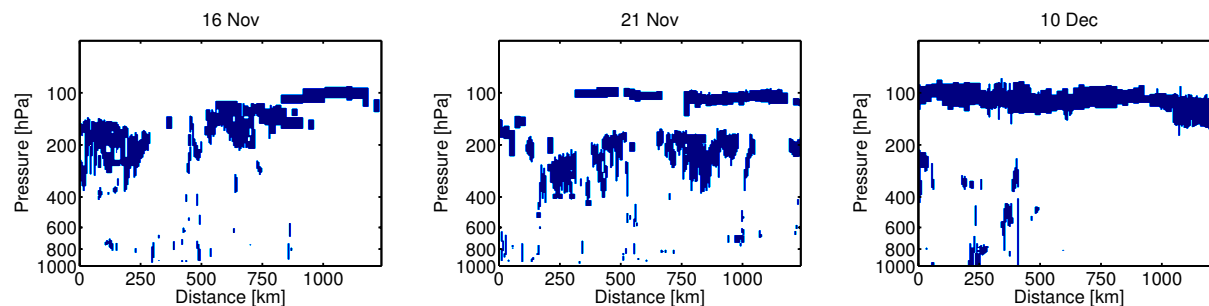
FIGURE 5.3. Examples of cloud layer fraction profiles, from 2011 CALIPSO satellite data during an overpass of a 10°-latitude x 10°-longitude box centered around Gan Island on 16 November, 21 November, and 10 December.

Due to different formation mechanisms cirrus cloud properties, including thickness and radiative properties, are variable throughout the time period. Figure 5.3 shows three examples of CALIPSO overpasses of Gan Island on 16 November, 21 November, and 10 December. Each indicates the presence of cirrus cloud during that time, though the individual profiles look quite different. Jensen et al. (1996) suggested that cirrus clouds near the tropical tropopause layer can be classified into two types: anvil cirrus clouds and in situ cirrus.

In situ cirrus clouds are formed when cold temperatures allow water vapor to either condense or form ice crystals in that region. The temperature changes are often a result of atmospheric wave processes or the hydrostatic response to deep convection. Convection clouds are found below thin cirrus in the 21 November profile. The cirrus on 10 December may also have tropospheric convection below, as the widespread cirrus appears optically thick and may have attenuated the signal. Anvil cirrus clouds are formed by detrainment from overshooting deep convective clouds in tropical regions and are typically long-lived due to greater moisture availability. The cloud profile on 16 November suggests this type of formation.

Figure 5.4 relates cirrus cloud occurrence to cold point tropopause temperatures at Gan and Manus. Generally, colder temperatures coincide with times when cirrus are present. This is particularly evident based on the shift in temperature range seen for Gan Island. At Manus Island, the CPT temperatures are colder overall, with the coldest CPT actually seen when cirrus clouds were absent in December. With the seasonal trend removed (not shown) the cold point temperatures found when cirrus are present do show a colder temperature range in comparison.
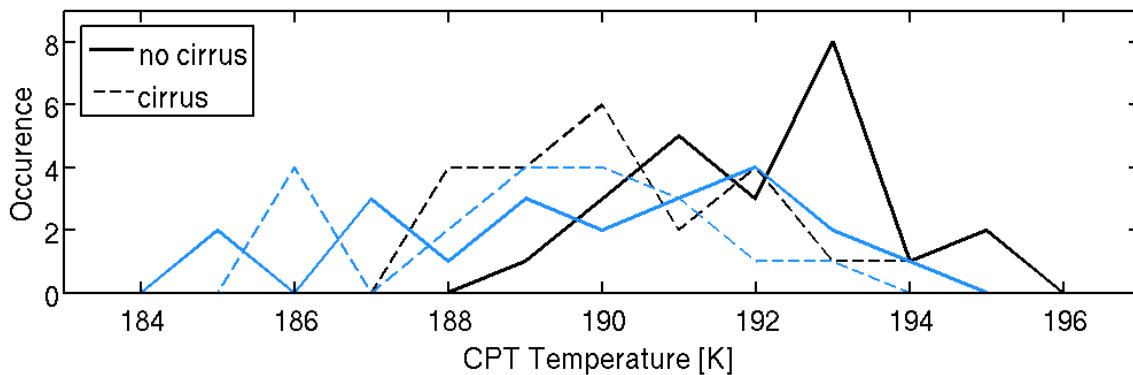

FIGURE 5.4. Histogram of cold point tropopause temperatures from 2011 DYNAMO atmospheric sounding data at Gan Island (black) and Manus Island (blue), in relation to CALIPSO cloud profiles where tropopause-level cirrus were either present (dashed) or absent (solid).

5.2. The missing effect in radiative heating rates

Previous studies have shown that clouds impact net radiative heating in the tropics, with implications for global climate. In the TTL, radiative heating rates can modulate troposphere-stratosphere transport. Impacts vary with cirrus cloud properties, such as optical thickness and if convective clouds are present. PNNL radiative heating rate profiles are used in this study to investigate these impacts on the TTL. However, as ground-based instrumentation were not able to detect high, thin clouds during DYNAMO, the full radiative effects are not included.

Figure 5.5a shows the mean net radiative heating rate profiles during the October to December time period, with both clear and full sky (clouds present) cases at Gan Island. Overall there is a net cooling in the troposphere peaking near the 300 hPa level, and warming aloft. The level of net zero radiative heating (LZRH) is near 125 hPa for both the clear sky and full sky. This is a typical level for clear sky conditions. On the other hand, prior research indicates that tropopause-level cirrus clouds absorb infrared radiation which leads to a localized warming and lowering of the LZRH by 0.5-1 km (Corti et al. 2005; Yang et al. 2010).

The mean net radiative heating for the clear sky case is shown with separated short-wave and longwave components. It is evident that the longwave cooling in the troposphere overwhelms the contribution from shortwave warming. The cloud radiative forcing changes this profile. A cooling or warming effect at each level is dependent on cloud interaction with outgoing longwave radiation and incoming solar radiation. The magnitude of absorption and reflection are dependent on the properties of the cloud. The net cloud radiative forcing for Gan shows an anomalous net warming in the troposphere and a cooling near cloud top. This net cooling between 150-200 hPa is in conflict the earlier studies (Corti et al. 2005; Yang et al. 2010), suggesting that the lack of cirrus clouds in the PNNL data creates a missing cirrus longwave heating component in the TTL. We would expect daily radiative profiles to reflect the cirrus seen in CALIPSO data, Figure 5.2, which is not the case.
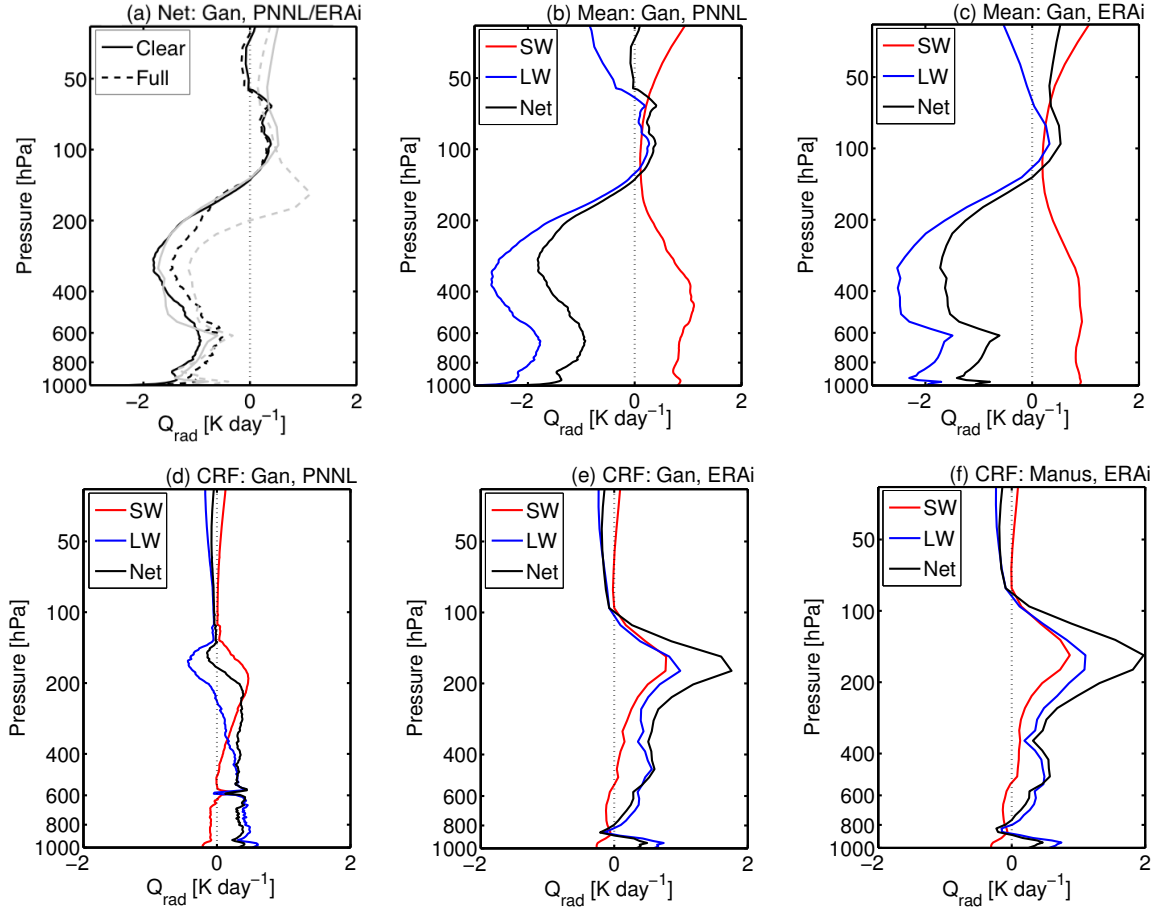
FIGURE 5.5. Mean vertical profiles of radiative heating rates. (a) Net radiative heating over Gan Island for clear sky (solid) and full sky (dashed) cases. PNNL (black) and ERAi (gray) data are shown for comparison. (b) Mean clear sky radiative heating over Gan Island separated into shortwave (red) and longwave (blue) components, from PNNL data. (c) Mean clear sky radiative heating over Gan Island, from ERAi data. (d) Mean cloud radiative forcing over Gan Island, from PNNL data. (e) Mean cloud radiative forcing over Gan Island, from ERAi data. (f) Mean cloud radiative forcing over Manus Island, from ERAi data.

For comparison to the PNNL results, the analysis was repeated using ERA-Interim data. The mean radiative heating profiles are similar, although ERA-Interim shows a significant lowering of the LZRH in the full sky case. With the PNNL data, there is no shift in the LZRH from the clear sky case to the addition of clouds. The ERA-Interim cloud radiative forcing profile shows a net warming of almost 2 K day^{-1} near 175 hPa. This is the expected net warming, but the magnitude of the value seems extreme. With ERA-Interim, there tends

to be a moist bias at upper-levels with potentially too much warming due to tropopause-level cirrus clouds (Wright and Fueglistaler 2013). Although there is no PNNL data for Manus, ERA-Interim data shows a stronger cloud radiative forcing based on higher cirrus occurrence in this region. This is consistent with the study by Yang et al. (2010) that found the maximum net cloud radiative heating is located over the west Pacific warm pool in boreal winter.

The Madden-Julian oscillation, which is characterized by enhanced deep convection and an increase in thin cirrus prior to peak convection, is expected to lower the LZRH and have impacts on vertical mass transport in the TTL. However, further analysis and data would be needed to determine this influence of the MJO on the TTL radiation heating, and to be able to compare these effects at Gan and Manus.

CHAPTER 6

CONCLUSIONS

6.1. SUMMARY OF RESULTS

The tropical tropopause layer is a transition region between the troposphere and stratosphere with multiscale variability that is not fully understood. Disturbances are found in anomalous temperature, wind and moisture fields as well as cirrus cloud occurrence ranging from a few days to an annual cycle. On intraseasonal timescales, TTL characteristics are modulated by the eastward-propagating Madden-Julian oscillation. In this study, we analyze high resolution data from the DYNAMO field campaign from October to December 2011. During this time period two prominent MJO events are seen, one in late October and the other in late November. Atmospheric soundings provide detailed vertical structure at upper levels not seen in meteorological analyses or in atmospheric models. We narrow our focus to two sites, Gan Island in the central Indian Ocean and Manus Island in the western Pacific Ocean, to determine how the large-scale MJO convective system impacts these sites locally as well as how they compare to one another. This allows us to study two distinct phases in the evolution of the MJO: modulation of the TTL during the initiation phase and during a mature phase as the MJO decouples from convection.

The Madden-Julian oscillation increases the frequency of overshooting convection into the TTL, with higher cloud top heights seen during the MJO active periods (Figure 3.6). A strong Kelvin wave cold phase is found above peak convection in the upper troposphere. Not only does this influence the depth of convection itself, but the cold point tropopause as well. CPT heights gradually lower following the descending cold anomaly, until the next cold phase descends from above and establishes a new CPT higher up (Figure 4.1). Lapse rate tropopause shows a similar trend but occurs lower in the atmosphere, and thus lags the CPT due to the downward phase velocity of the Kelvin wave.

It is clear from temperature and wind anomalies that wave activity is prevalent during DYNAMO with multiscale variability in the TTL. Waves are generated in the troposphere by convection and vertically propagate to the stratosphere, providing a dynamical coupling between the two regions. The observed vertical propagation in the TTL is due to the greater stratification of the background atmosphere. Spectral filtering was used to separate Kelvin waves from higher frequency gravity waves (Figures 4.6 and 4.7). Zonal wind and temperature anomalies are nearly in quadrature, as expected from linear wave theory. The downward phase velocity and eastward tilt with height are consistent with upward energy dispersion from an eastward propagating energy source below.

Convectively-coupled equatorial Kelvin waves are found in the 100-150 hPa layer at Gan Island during both MJO active periods. The large planetary-scale wave seen in the lower stratosphere in late October is likely a free wave mode unrelated to MJO dynamics. The two wave types are separated by a strong zonal wind shear at 90 hPa transitioning to a QBO westerly wind regime in the lower stratosphere. In addition to Kelvin waves, there is substantial gravity wave activity throughout the time period. Analysis of lower stratospheric wave energy did not reveal dependency on MJO phase (Figure 4.8), with similar gravity wave energy density amplitudes during the MJO convective and suppressed periods.

Large-scale convection leads to an equatorial wave response in the TTL that creates favorable conditions for cirrus cloud formation. In particular, a Kelvin wave cold phase can establish higher relative humidity levels that are mirrored by increased cirrus cloud frequency preceding MJO peak convection (Figure 5.1). This is where temperatures are cold enough to support ice cloud formation, suggesting a dependence on TTL thermodynamic structure. Upper-level cirrus, in addition to MJO-related deep convective clouds, impact radiative heating rates through localized warming and act to lower the level of zero net radiative heating. Unfortunately, realistic net heating associated with cirrus clouds could not be incorporated into PNNL radiative retrievals (Figure 5.5) as they did not have instrumentation on Gan to fully sample the cirrus cloud coverage. This is left for future research.

This observational study on the tropical tropopause layer and how it is modulated by the Madden-Julian oscillation on intraseasonal timescales has contributed to our understanding of water vapor variability at upper levels. Water vapor variability in the lower stratosphere may influence surface temperatures through the impact on the Earth's radiative balance. The MJO increases troposphere-stratosphere exchange directly through a higher cloud top heights which may be linked to overshooting convection and moistening of the stratosphere. In contrast, cirrus cloud formation plays a critical role in dehydration through freeze-drying processes. Atmospheric waves, which are primarily generated by large-scale MJO convection in the troposphere, determine the conditions for cirrus cloud formation. Cirrus clouds can also be generated directly by convective outflow aloft. Modulation by the MJO is dependent on location and regional climatology. Located in the region of MJO initiation, Gan Island shows strong anomalous wave activity in the TTL. In general, features are less pronounced and appear later at Manus Island, as the MJO decouples from convection and loses strength during its eastward-propagation into the western Pacific Ocean.

6.2. Future work

There are several limitations to this study, one of which is that only two sites were considered. The evolution of upper level features during the propagation from the central Indian Ocean to the western Pacific must be inferred from the initial and final conditions alone. With two point locations the horizontal extent of the TTL disturbances can also not be established. Including an array of observations over a greater spatial domain in the analysis may lead to more robust results tied to the large-scale impact of the MJO, rather than a focus on what may be a localized response. Furthermore, this study has only utilized one dataset that features two MJOs. We must be cautious about making generalizations on the modulation of the TTL by the MJO with this limited sample size. Particularly because the two MJO were quite different themselves. A case study approach is informative and a great use of this dataset because of the high resolution, but results may be unique to DYNAMO. For example, results during La Niña conditions may not apply in the warm

phase of ENSO, and Manus Island observations may look significantly different in subsequent years. Additionally, the radiative heating rate analysis is limited by the lack of tropopause-level cirrus clouds in the ground-based observations, and leads to inaccurate estimations of radiative heating rate profiles associated with the MJO. These research limitations and the results of the study point to several directions for future work.

An extension of this research for further consideration is analysis of the planetary-scale Kelvin wave in the lower stratosphere. Why is it that a wave of this nature is present during the first MJO active period and not the second? How is this wave different from the Kelvin waves below the cold point tropopause, which do appear to interact with MJO convection? Ray tracing methods, as used by Flannaghan and Fueglistaler (2013), could be used to determine the origin of the wave. This would help clarify if the initial energy source of the wave is the MJO, or if the wave is indeed a dry wave mode free from forcings below. Extending the analysis to incorporate more observational sites, including those off of the equator, could give us a better idea of the spatial scale and bring out horizontal waves features. It is also worthwhile to consider how it is that the Kelvin wave is able to persist in a background westerly wind regime of the QBO, as well as the role of westerly wind shear. Though Kelvin waves are able to propagate in weak westerlies, they are likely to dissipate as they approach a critical background mean flow.

Gravity wave variability throughout the DYNAMO time period is another opportunity for future work. In this study, wave activity does not appear to be enhanced by the MJO, as we might expect. Further analysis could be done to quantify the momentum flux and wave-induced force that is alluded to in Section 4.3, but is not fully addressed in this study. Studies such as Eckermann (1996) and Serafimovich et al. (2005), use the hodograph method to investigate gravity wave properties, plotting zonal and meridional wind anomalies over a vertical layer against each other. This method could be used for the DYNAMO dataset on the lower stratospheric horizontal wind anomalies which have been filtered with a 7 day highpass. Gravity wave activity would be seen as an elliptical pattern in the hodograph. Characteristics such as the sense of rotation with height and the ratio of axes, provides

information on properties of the wave field, including intrinsic frequency, wavelength, and propagation direction. It is possible that these gravity wave characteristics reveal modulation by the MJO.

Since the effects of tropopause-level cirrus clouds were not incorporated in the PNNL radiative transfer calculations, the next step would be to include these effects. This would involve modifying radiative heating rate code in order to include DYNAMO background conditions, as well as time-varying cirrus cloud properties. In this study, the presence of cirrus clouds was determined based on a rough set of guidelines. In future work, it would be beneficial to define specific criteria in their identification. A good option might be to follow the method for ice cloud detection used by Martins et al. (2011). This detection is based on a minimum threshold for particulate backscatter signal, a horizontal extent of 20 km or more, and requires a minimum vertical extent of 240 m. Furthermore, we could take typical cirrus cloud properties into consideration, such as cloud top temperature, optical depth, as well as particulate depolarization ratios, which are used to distinguish water droplets from ice crystals. With these criteria we would be able to investigate how different cloud parameters affect TTL radiative heating rates throughout the DYNAMO field campaign.

REFERENCES

Alexander, M. J., and J. R. Holton, 1997: A model study of zonal forcing in the equatorial stratosphere by convectively induced gravity waves. *J. Atmos. Sci.*, **54,** 408-419.

Allen, S., and R. A. Vincent, 1995: Gravity wave activity in the lower atmosphere: Seasonal and latitudinal variations. *J. Geophys. Res.*, **100,** 1327-1350.

Andrews, D. G., J. R. Holton, and C. B. Leovy, 1987: *Middle Atmosphere Dynamics*. Academic Press, 489 pp.

Baldwin, M. P., L. J. Gray, T. J. Dunkerton, K. Hamilton, P. H. Haynes, W. J. Randel, J. R. Holton, M. J. Alexander, I. Hirota, T. Horinouchi, D. B. A. Jones, J. S. Kinnersley, C. Marquardt, K. Sato, and M. Takahashi, 2001: The Quasi-Biennial Oscillation. *Rev. Geophys.*, **39,** 179-229.

Boehm, M. T., and J. Verlinde, 2000: Stratospheric influence on upper tropospheric tropical cirrus. *Geophys. Res. Lett.*, **27,** 3209-3212.

Booker, J. R. and F. P. Bretherton, 1967: The critical layer for internal gravity waves in a shear flow. *J. Fluid Mech.*, **27,** 513-539.

Bohren, C. F. and B. A. Albrecht, 1998: *Atmospheric Thermodynamics*. Oxford University Press, 402 pp.

Brewer, A. W., 1949: Evidence for a world circulation provided by the measurements of helium and water vapour distribution in the stratosphere. *Quart. J. Roy. Meteor. Soc.*, **75,** 351-363.

Ciesielski, P. E., H. Yu, R. H. Johnson, K. Yoneyama, M. Katsumata, C. N. Long, J. Wang, S. M. Loehrer, K. Young, S. F. Williams, W. Brown, J. Braun, T. Van Hove, 2014: Quality-controlled upper-air sounding dataset for DYNAMO/CINDY/AMIE: Development and corrections. *J. Atmos. Oceanic Technol.*, **31,** 741-764.

Corti, T., B. P. Luo, T. Peter, H. Vömel, and Q. Fu, 2005: Mean radiative energy balance and vertical mass flux in the equatorial upper troposphere and lower stratosphere.*Geophys. Res. Lett.*, **32,** L06802.

Corti, T., B. P. Luo, Q. Fu, H. Vömel, and T. Peter, 2006: The impact of cirrus clouds on tropical troposphere to stratosphere transport. *Atmos. Chem. Phys.*,**6,** 2539-2547.

Del Genio, A. D., Y.-H. Chen, D. Kim, and M.-S. Yao, 2012: The MJO transition from shallow to deep convection in *CloudSat/CALIPSO* data and GISS GCM simulations.*J. Climate*, **25,** 3755-3770.

Dobson, G. M. B., 1956: Origin and distribution of polyatomic molecules in the atmosphere. *Proc. Roy. Soc. London*, **A236,** 187-193.

Eckermann, S. D., 1996: Hodographic analysis of gravity waves: Relationships among Stokes parameters, rotary spectra, and cross-spectral methods. *J. Geophys. Res.*, **101,** 19169-19174.

Eguchi, N., and M. Shiotani, 2004: Intraseasonal variations of water vapor and cirrus clouds in the tropical upper troposphere, *J. Geophys. Res.*, **109,** D12106.

Feng Z., S. A. McFarlane, C. Schumacher, S. Ellis, J. M. Comstock, and N. Bharadwaj, 2014: Constructing a merged cloud-precipitation radar dataset for tropical convective clouds during the DYNAMO/AMIE experiment at Addu Atoll. *J. Atmos. Oceanic Technol.*, **31,** 1021-1042.

Flannaghan, T. J., and S. Fueglistaler, 2013: The importance of the tropical tropopause layer for equatorial Kelvin wave propagation, *J. Geophys. Res. Atmos.*, **118,** 5160-5175.

Fovell, R., D. Durran, and J. R. Holton, 1992: Numerical simulations of convectively generated stratospheric gravity waves. *J. Atmos. Sci.*, **49,** 1427-1442.

Fueglistaler, S., A. E. Dessler, T. J. Dunkerton, I. Folkins, Q. Fu, and P. W. Mote, 2009a: Tropical tropopause layer. *Rev. Geophys.*, **47,** RG1004.

Fujiwara, M., and Coauthors, 2009: Cirrus observations in the tropical tropopause layer over the western Pacific. *J. Geophys. Res.*, **114,** D09304.

Fujiwara, M., J. Suzuki, A. Gettelman, M. I. Hegglin, H. Akiyoshi, and K. Shibata, 2012: Wave activity in the tropical tropopause layer in seven reanalysis and four chemistry climate model data sets, *J. Geophys. Res.*, **117,** D12105.

Garand, L., C. Grassotti, J. Hall, and G. L. Klein, 1992: On differences in radiosonde humidity-reporting practices and their implications for numerical weather prediction and remote sensing. *Bull. Amer. Meteor. Soc.*, **73,** 1417-1423.

Gill, A. E., 1980: Some simple solutions for heat induced tropical circulation. *Quart. J. Roy. Meteor. Soc.*, **106,** 447-462.

Gill, A. E., 1982: *Atmosphere-Ocean Dynamics.* Academic Press, 662 pp.

Grise, K. M., D. W. J. Thompson, and T. Birner, 2010: A global survey of static stability in the stratosphere and upper troposphere. *J. Climate*, **23,** 2275-2292.

Grise, K. M., and D. W. J. Thompson, 2013: On the signatures of equatorial and extratropical wave forcing in tropical tropopause layer temperatures. *J. Atmos. Sci*, **69,** 857-874.

Hendon, H. H., M. L. Salby, 1994: The Life Cycle of the Madden-Julian Oscillation. *J. Atmos. Sci.*, **51,** 2225-2237.

Holloway, C. E. and J. D. Neelin, 2007: The convective cold top and quasi equilibrium. *J. Atmos. Sci.*, **64,** 1467-1487.

Holton, J. R. and G. J. Hakim, 2013: *An Introduction to Dynamic Meteorology.* Fifth edition. Elsevier Academic Press, 532 pp.

Holton, J. R., P. H. Haynes, M. E. McIntyre, A. R. Douglass, R. B. Rood, and L. Pfister, 1995: Stratosphere-troposphere exchange. *Rev. Geophys.*, **33,** 403-439.

Holton, J. R., M. J. Alexander, and M. T. Boehm, 2001: Evidence for short vertical wavelength Kelvin waves in the Department of Energy-Atmospheric Radiation Measurement Nauru99 radiosonde data. *J. Geophys. Res.*, **106,** 20,125-20,129.

Jensen, E. J., O. B. Toon, L. Pfister, and H. B. Selkirk, 1996: Dehydration of the upper troposphere and lower stratosphere by subvisible cirrus clouds near the tropical tropopause. *Geophys. Res. Lett.*, **23,** 825-828.

Jiang, X., D. E. Waliser, W. S. Olson, W.-K. Tao, T. S. L'Ecuyer, K.-F. Li, Y. L. Yung, S. Shige, S. Lang, and Y. N. Takayabu, 2011: Vertical diabatic heating structure of the MJO: Intercomparison between recent reanalyses and TRMM estimates. *Mon. Wea. Rev.*, **139,** 3208-3223.

Johnson, R. H., and D. C. Kriete, 1982: Thermodynamic and circulation characteristics of winter monsoon tropical mesoscale convection. *Mon. We. Rev.*, **110,** 1898-1911.

Johnson, R. H., and P. E. Ciesielski, 2013: Structure and properties of Madden-Julian oscillations deduced from DYNAMO sounding arrays. *J. Atmos. Sci.*, **70,** 3157-3179.

Johnson, R. H., P. E. Ciesielski, J. H. Ruppert, Jr., and M. Katsumata, 2014: Sounding-based thermodynamic budgets for DYNAMO. *J. Atmos. Sci.*, in press.

Kiladis, G. N., J. Dias, K. H. Straub, M. C. Wheeler, S. N. Tulich, K. Kikuchi, K. M. Weickmann, and M. J. Ventrice, 2014: A comparison of OLR and circulation-based indices for tracking the MJO. *Mon. Wea. Rev.*, **142,** 1697-1715.

Kiladis, G. N., K. M. Weickmann, 1992: Extratropical forcing of tropical Pacific convection during northern winter. *Mon. Wea. Rev.*, **120,** 1924-1938.

Kiladis, G. N., K. H. Straub, G. C. Reid, and K. S. Gage, 2001: Aspects of interannual and intraseasonal variability of the tropopause and lower stratosphere. *Quart. J. Roy. Meteor. Soc.*, **127,** 1961-1984.

Kiladis, G. N., M. C. Wheeler, P. T. Haertel, K. H. Straub, and P. E. Roundy, 2009: Convectively coupled equatorial waves. *Rev. Geophys.*, **47,** RG2003.

Kim, J. and S.-W. Son, 2012: Tropical Cold-Point Tropopause: Climatology, Seasonal Cycle, and Intraseasonal Variability Derived from COSMIC GPS Radio Occultation Measurements. *J. Climate*, **25,** 5343-5360.

Leena, P. P., M. Venkat Ratnam, B. V. Krishna Murthy, and S. Vijaya Bhaskara Rao, 2012: Detection of high frequency gravity waves using high resolution radiosonde observations. *J. Atmos.-Sol. Terr. Phys.*, **77,** 254-259.

Liou, K-N, 1986: Influence of Cirrus Clouds on Weather and Climate Processes: A Global Perspective. *Mon. Wea. Rev.*, **114,** 1167-1199.

Long, C. S. and J. R. Christy, 2014: [Temperature] Lower Stratospheric Temperature [in State of the Climate in 2013]. *Bull. Amer. Meteor. Soc.*, **95** (7), S14-S15.

Madden, R., and P. Julian, 1971: Detection of a 40-50-day oscillation in the zonal wind in the tropical Pacific. *J. Atmos. Sci.*, **28,** 702-708.

Madden, R. A., and P. R. Julian, 1972: Description of global-scale circulation cells in the Tropics with a 40-50 day period. *J. Atmos. Sci*, **29,** 1109-1123.

Martins, E., V. Noel, and H. Chepfer, 2011: Properties of cirrus and subvisible cirrus from nighttime Cloud-Aerosol Lidar with Orthogonal Polarization (CALIOP), related to atmospheric dynamics and water vapor. *J. Geophys. Res.*, **116,** D02208.

Mote, P., and Coauthors, 1996: An atmospheric tape recorder: The imprint of tropical tropopause temperatures on stratospheric water vapor. *J. Geophys. Res.*, **101,** 3989-4006.

Matsuno, T., 1966: Quasi-geostrophic motions in the equatorial area. *J. Meteor. Soc. Japan*, **44,** 25-43.

Paulik, L. C. and T. Birner, 2012: Quantifying the deep convective temperature signal within the tropical tropopause layer (TTL). *Atmos. Chem. Phys.*, **12,** 12183-12195.

Peatman, S. C., A. J. Matthews, and D. P. Stevens, 2014: Propagation of the Madden-Julian Oscillation through the Maritime Continent and scale interaction with the diurnal cycle of precipitation. *Q.J.R. Meteorol. Soc.*, **140,** 814-825.

Randel, W. J., and E. J. Jensen, 2013: Physical processes in the tropical tropopause layer and their roles in a changing climate. *Nature Geoscience*, **6,** 169-176.

Randel, W. J., F. Wu, and D. J. Gaffen, 2000: Interannnual variability of the tropical tropopause derived from radiosonde data and NCEP reanalyses, *J. Geophys. Res.*, **105(D12),** 15509-15523.

Sandor, B. J., E. J. Jensen, E. M. Stone, W. G. Read, J. W. Waters, and J. L. Mergenthaler, 2000: Upper tropospheric humidity and thin cirrus, *Geophys. Res. Lett.*, **27,** 2645-2648.

Sassen, K., Z. Wang, and D. Liu, 2008: Global distribution of cirrus clouds from CloudSat/ Cloud-Aerosol Lidar and Infrared Pathfinder Satellite Observations (CALIPSO) measurements. *J. Geophys. Res.*, **113,** D00A12.

Serafimovich, A., P. Hoffmann, D. Peters, and V. Lehmann, 2005: Investigation of inertia-gravity waves in the upper troposphere/lower stratosphere over northern Germany observed with collocated VHF/UHF radars. *Atmos. Chem. Phys. Discuss.*, **5,** 295-310.

Sherwood, S. C., and R. Wahrlich, 1999: Observed evolution of tropical deep convective events and their environment. *Mon. Wea. Rev.*, **127,** No. 8, 1777-1795.

Sherwood, S. C., T. Horinouchi and H.A. Zeleznik, 2003: Convective impact on temperatures observed near the tropical tropopause. *J. Atmos. Sci.*, **60,** No. 15, 1847-1856.

Shindell, D. T., 2001: Climate and ozone response to increased stratospheric water vapor. *Geophys. Res. Lett.*, **28,** 1551-1554.

Sobel, A. H., and E. D. Maloney, 2013: Moisture modes and the eastward propagation of the MJO. *J. Atmos. Sci.*, **70,** 187-192.

Solomon, S., K. H. Rosenlof, R. W. Portmann, J. S. Daniel, S. M. Davis, T. J. Sanford, and G.-K. Plattner, 2010: Contributions of stratospheric water vapor to decadal changes in the rate of global warming. *Science*, **327,** 1219-1223.

Straub, K. H., and G. N. Kiladis, 2002: Observations of a Convectively Coupled Kelvin Wave in the Eastern Pacific ITCZ. *J. Atmos. Sci.*, **59,** 30-53.

Suzuki, J., M. Fujiwara, A. Hamada, Y. Inai, J. Yamaguchi, R. Shirooka, F. Hasebe, and T. Takano, 2010: Cloud-top height variability associated with equatorial Kelvin waves in the tropical tropopause layer during the Mirai Indian Ocean cruise for the Study of the MJO-convection Onset (MISMO) campaign. *SOLA*, **6,** 97-100.

Suzuki, J., M. Fujiwara, T. Nishizawa, R. Shirooka, K. Yoneyama, M. Katsumata, I. Matsui, and N. Sugimoto, 2013: The occurrence of cirrus clouds associated with eastward propagating equatorial n=0 inertio-gravity and Kelvin waves in November 2011 during the CINDY2011/DYNAMO campaign. *J. Geophys. Res. Atmos.*, **118,** 12941-12947.

Tian, B., C. O. Ao, D. E. Waliser, E. J. Fetzer, A. J. Mannucci, and J. Teixeira, 2012: Intraseasonal temperature variability in the upper troposphere and lower stratosphere from the GPS radio occultation measurements. *J. Geophys. Res.*, **117,** D15110.

Ventrice, M. J., M. C. Wheeler, H. H. Hendon, C. J. Schreck, C. D. Thorncroft, and G. N. Kiladis, 2013: A modified multivariate Madden-Julian oscillation index using velocity potential. *Mon. Wea. Rev.*, **141,** 4197-4210.

Virts, K. S., and J. M. Wallace, 2010: Annual, interannual, and intraseasonal variability of tropical tropopause transition layer cirrus. *J. Atmos. Sci.*, **67,** 3097-3112.

Virts, K. S., and J. M. Wallace, 2014: Observations of temperature, wind, cirrus, and trace gases in the tropical tropopause transition layer during the MJO. *J. Atmos. Sci*, **71,** 1143-1157.

Virts, K. S., J. M. Wallace, Q. Fu, and T. P. Ackerman, 2010: Tropical tropopause transition layer cirrus as represented by *CALIPSO* lidar observations. *J. Atmos. Sci.*, **67,** 3113-3129.

Wallace, J. M., 1971: Spectral studies of tropospheric wave disturbances in the tropical Western Pacific. *Rev. Geophys.*, **9,** 557-612.

Wang, L., and M. A. Geller, 2003: Morphology of gravity wave energy as observed from 4 years (1998-2001) of high vertical resolution U.S. radiosonde data. *J. Geophys. Res.*, **108,** 4489.

Wheeler, M. C., and H. H. Hendon, 2004: An all-season real-time multivariate MJO index: Development of an index for monitoring and prediction. *Mon. Wea. Rev.*, **132,** 1917-1932.

Wheeler, M., and G. N. Kiladis, 1999: Convectively coupled equatorial waves: Analysis of clouds and temperature in the wavenumber-frequency domain. *J. Atmos. Sci.*, **56,** 374-399.

Wheeler, M., G. N. Kiladis, and P. J. Webster, 2000: Large-scale dynamical fields associated with convectively coupled equatorial waves. *J. Atmos. Sci.*, **57,** 613-640.

Winker, D., W. Hunt, and M. McGill, 2007: Initial performance assessment of CALIOP, 2007. *Geophys. Res. Lett.*, **34,** L19803.

Wright, J.S. and S. Fueglistaler, 2013: Large Differences in the Diabatic Heat Budget of the Tropical UT/LS in Reanalyses. *Atmos. Chem. Phys.*, **13,** 9565-9576.

Yano, J.-I. and Marine Bonazzola, 2009: Scale Analysis for Large-Scale Tropical Atmospheric Dynamics. *J. Atmos. Sci.*, **66,** 159-172.

Yoneyama, K., C. Zhang, and C. N. Long, 2013: Tracking pulses of the Madden-Julian oscillation. *Bull. Amer. Meteor. Soc.*, **94,** 1871-1891.

Yulaeva, E., J. Holton, and J. M. Wallace, 1994: On the cause of the annual cycle in tropical lower-stratospheric temperatures. *J. Atmos. Sci.*, **51,** 169-174.

Zeng, Z., S.-P. Ho, S. Solkolovskiy, and Y.-H. Kuo, 2012: Structural evolution of the Madden-Julian Oscillation from COSMIC radio occultation data. *J. Geophys. Res.*, **117,** D22108.

Zhang, C., 2005: Madden-Julian Oscillation. *Rev. Geophys.*, **43,** RG2003.

Zhang, C., 2013: Madden-Julian Oscillation: Bridging Weather and Climate. *Bull. Amer. Meteor. Soc.*, **94,** 1849-1870.

Zhang, S. D., F. Yi, C. M. Huang, K. M. Huang, Y. Gong, Q. Gan, and Y. H. Zhang, 2013: Latitudinal and altitudinal variability of lower atmospheric inertial gravity waves revealed by U.S. radiosonde data. *J. Geophys. Res. Atmos.*, **118,** 1-15.